Patient-specific fracture risk assessment of vertebrae: A multiscale approach coupling X-ray physics and continuum micromechanics

Romane Blanchard, Claire Morin, Andrea Malandrino, Alain Vella, Zdenka Sant, Christian Hellmich

INTERNATIONAL JOURNAL FOR NUMERICAL METHODS IN BIOMEDICAL ENGINEERING
Int. J. Numer. Meth. Biomed. Engng. (2016); e02760
Published online in Wiley Online Library (wileyonlinelibrary.com). DOI: 10.1002/cnm.2760

Patient-specific fracture risk assessment of vertebrae: A multiscale approach coupling X-ray physics and continuum micromechanics

Romane Blanchard[1], Claire Morin[2], Andrea Malandrino[3], Alain Vella[4], Zdenka Sant[4] and Christian Hellmich[1,*,†]

[1] *TU Wien–Vienna University of Technology, Institute for Mechanics of Materials and Structures, Karlsplatz 13/202, Vienna 1040, Austria*
[2] *CIS-EMSE, CNRS:UMR 5307, LGF, Ecole Nationale Supérieure des Mines, Saint-Etienne F-42023, France*
[3] *Institute for Bioengineering of Catalonia, C/Baldiri Reixac 10–12, Barcelona 08028, Spain*
[4] *Mechanical Engineering Department, University of Malta, Tal Qroqq, Msida MSD 2080, Malta*

SUMMARY

While in clinical settings, bone mineral density measured by computed tomography (CT) remains the key indicator for bone fracture risk, there is an ongoing quest for more engineering mechanics-based approaches for safety analyses of the skeleton. This calls for determination of suitable material properties from respective CT data, where the traditional approach consists of regression analyses between attenuation-related grey values and mechanical properties.

We here present a physics-oriented approach, considering that elasticity and strength of bone tissue originate from the material microstructure and the mechanical properties of its elementary components. Firstly, we reconstruct the linear relation between the clinically accessible grey values making up a CT, and the X-ray attenuation coefficients quantifying the intensity losses from which the image is actually reconstructed. Therefore, we combine X-ray attenuation averaging at different length scales and over different tissues, with recently identified 'universal' composition characteristics of the latter.

This gives access to both the normally non-disclosed X-ray energy employed in the CT-device and to *in vivo* patient-specific and location-specific bone composition variables, such as voxel-specific mass density, as well as collagen and mineral contents. The latter feed an experimentally validated multiscale elastoplastic model based on the hierarchical organization of bone. Corresponding elasticity maps across the organ enter a finite element simulation of a typical load case, and the resulting stress states are increased in a proportional fashion, so as to check the safety against ultimate material failure. In the young patient investigated, even normal physiological loading is probable to already imply plastic events associated with the hydrated mineral crystals in the bone ultrastructure, while the safety factor against failure is still as high as five.

Received 14 October 2015; Accepted 15 October 2015

KEY WORDS: X-ray physics; bone mass density; spine; bone; strength; continuum micromechanics; elastoplasticity.

1. INTRODUCTION

The broad scattering of ultimate forces bearable by human vertebrae [1–4] has motivated the quest for indicators of the actual, that is, patient-specific, strength exhibited by a particular vertebral body of interest, and the most accepted indicator in this context remains the 'bone mineral density – BMD' [5, 6]. However, it is much less clear how and to which extent BMD (alone) would govern bone fracture risk, and there is an ongoing discussion on additional or alternative risk indicators [7–12], based on quite comprehensive statistical analyses. At the same time, it is clearly felt that an

*Correspondence to: Christian Hellmich, TU Wien–Vienna University of Technology, Institute for Mechanics of Materials and Structures, Karlsplatz 16, Vienna 1040, Austria.
†E-mail: christian.hellmich@tuwien.ac.at

engineering mechanics-based assessment of fracture risk, as it is the basis for structural design in civil and mechanical engineering, should hold the capacity to overcome the shortcomings of the purely statistics-based and population-related approaches referred to earlier. Accordingly, computed tomography (CT)-based and finite element-based failure risk assessment of bony structures remains one of the central desires in bone biomechanics. This topic has been dealt with extensively, but broad clinical application has not been achieved yet. The reason for this could be that the physical origins of bone strength may need to be considered more deeply and rigorously than it has been attempted so far. In fact, when screening the comprehensive literature on the topic, it becomes obvious that even the most famous contributions on the topic rely on purely elastic analyses. Typically, linear regression parameters between linear elastic FE analyses and strength tests performed on the same piece of bone are established, which are typically superior to regressions between strength and some direct radiological measures [3, 13, 14]. In other studies, stress states derived from linear finite element analyses are averaged over suitably chosen 'regions of interest', and corresponding average stress levels are thought to be relevant for fracture risk assessment [15]. Still, one might argue that the choice of such regions of interest may be quite arbitrary, but at the same time very influential on the corresponding simulation results. This would call for a deeper theoretical involvement into the material mechanics of bone, and a particularly notable approach was realized for human femura [16, 17], where a certain consensus has been gained in the community as regards to CT-to-mechanics calibration schemes [18–20]. Namely, elastic properties derived from CT-based and mass density-based calibration schemes [21–24] are mapped onto finite element meshes, and for a variety of load cases, strains as obtained from an elastic simulation are assessed with respect to a failure criterion based on a constant maximum principal strain. The aforementioned consensus (or even enough data for potentially reaching it) is hard to find for other types of bone where only very few studies exist [25], so that again deeper theoretical understanding is necessary, the obvious next step thereby concerning elastoplasticity. In fact, elastoplastic finite element simulations on bony organs have already been performed [26], and they have turned out to be useful when it comes to simulate the interaction between an implant and the neighboring bone. Still, this does not render the entire issue of bone strength assessment as being solved. There is a second challenge, which needs to be overcome: the determination of relevant mechanical properties (elastic as well as elasto-plastic strength values), from clinically available CT images. The traditional approach [15] consists of regression analyses between attenuation-related grey values and mechanical properties; however, no consensus exists on unique regression parameters. They most probably depend on various additional variables, such as CT machine settings and X-ray energies used. Still, such empirical density-stiffness relations are also used in an inverse fashion, in order to relate elastic property distributions across organs to corresponding mass densities [27]. In this case, the elastic property distributions were determined such that given physiological load cases resulted in targeted strain magnitudes as proposed in the framework of the Mechanostat theory [28]. On the other hand, a more physics-oriented approach would ask for the origin of elasticity and strength of the material found within each voxel to be found in a computed tomograph – this origin being the material microstructure and the mechanical properties of its elementary components, in the case of bone: hydroxyapatite, collagen, and water with some non-collageneous organics. Thanks to recent discoveries concerning universal patterns in bone tissue composition and microstructure [29–32], as well as their effects on the tissue's elasticity and strength [33–35], we are now in the position to rigorously relate tissue mass densities and porosities at different scales of observation, to corresponding elastic and strength values. Still, these mass densities need to be related to the grey values defining a CT-image, in order to obtain the desired (unique and reliable) relation between CT-numbers and mechanical properties. In this context, it proved useful to translate the chemical characteristics (and hence the mass density) of the matter found in each and every voxel making up a 3D stack of CT images, into the corresponding X-ray attenuation coefficients, based on the publicly available National Institute of Standards and Technology (NIST) database [36] and the average rule for attenuation coefficients [18, 37–43]. However, such a determination of density/chemistry-attenuation relations is often challenged by the fact that the X-ray attenuation coefficients do not only depend on the material's chemistry (which establishes a link to mass density) but also on the X-ray energy used for the CT image, and as a rule, the latter is not documented in a clinical setting. Extending, modifying, and adapting recent results gained

DOI: 10.1002/cnm

in the context of ceramic biomaterials [44], the present paper describes, by example of a human vertebra, how to overcome this last obstacle, through combining X-ray attenuation averaging at different scales and over different tissues, with 'universal' compositional characteristics of the latter. This opens the way to fully patient-specific and site-specific mass density and composition maps throughout the investigated organs. Using this composition as input for mathematically cast explicit quantification of the hierarchical microstructure of bone and its effect on the unique mechanical properties of this biological material will finally allow us to extend a safety assessment philosophy, which is used very successfully in everyday steel or concrete engineering, towards the needs of a very intricate life science problem: the breaking of bones.

As regards the use of fundamental principles, X-ray physics-derived (voxel-specific) mineral, collagen, and water contents for a human vertebra will be fed into a homogenization theory-based multiscale mechanics representation of bone [34, 35], which has been extensively validated experimentally for both elastic and strength properties. This will provide calibration-free and phantom-free conversion of CT data into mechanical properties.

As regards the safety assessment concept, voxel-specific elastic properties gained by means of the aforementioned conversion method will enter linear elastic finite element simulations, so as to deliver organ-wide stress distributions related to a typical load case. These local, that is, element-specific, stress states are subsequently increased in a proportional fashion, so as to check which elastoplastic events would develop in the hydrated mineral crystals, before brittle fracture of molecular collagen would mark ultimate material failure. The corresponding proportionality factors quantify the element-specific safety against fracture, which is a lower bound to the overall organ fracture risk.

2. MATERIALS AND METHODS

2.1. Conversion of CT grey values into energy–dependent attenuation coefficients, based on statistical image evaluation and on soft tissue composition rules

A CT scan of a motion segment of a 15-years-old male patient, consisting of two lumbar vertebral bodies L3 and L4, was obtained from Mater Dei Hospital, Malta. The HiSpeed Dual medical CT scanner from General Electrics was employed in helical mode, with the following parameters: source voltage, 140 kV; source current, 110 μA; exposure time, 1000 ms; image pixel size, 0.324 mm; and slice spacing, 1.25 mm. In the respective CT images, which capture not only the bone structure of a vertebral body, but also the surrounding soft tissue, the X-ray attenuation information is stored in terms of 8-bit grey values, increasing with intensifying attenuation. In order to separate soft and hard tissues, all the grey values found in the 3D image are evaluated first in terms of a (normalized) histogram, representing a probability density function for the grey value of one voxel which is randomly chosen from the 3D image. More precisely, in such a histogram, we identify two peaks related to the most frequently occurring grey values, containing (i) adipose tissues (GV_{fat}) and (ii) inner organs (GV_{soft}), with $GV_{fat} < GV_{soft}$. In order to separate bone tissue voxels from their surroundings, we consider the first minimum value of the probability density function, which appears on the right-hand side of GV_{soft}, that is, for $GV > GV_{soft}$. We denote this minimum value as segmentation threshold GV_{thr}.

In order to back-translate the user-selected grey scale values into the underlying X-ray attenuation values, we consider the linear relation between grey values and X-ray energy-dependent attenuation coefficients, involving three unknowns: two proportionality factors a and b, and the X-ray energy $\mathcal{E}$ as follows [45]:

$$\mu(\mathcal{E}) = a(\mathcal{E}) \times GV + b(\mathcal{E}). \tag{1}$$

Equation (1) expresses that the X-ray attenuation coefficient is no classical material property; namely, it depends not only on the matter contained in a specific voxel but also on the energy used for the X-ray penetration of the investigated object. In order to identify the energy-dependent slope and intercept functions, $a(\mathcal{E})$ and $b(\mathcal{E})$, we specify (1) for the aforementioned two landmark values concerning fat and soft tissues:

DOI: 10.1002/cnm

$$\mu_{fat}(\mathcal{E}) \quad = a(\mathcal{E}) \times GV_{fat} + b(\mathcal{E}) \tag{2}$$

$$\mu_{soft}(\mathcal{E}) \; = a(\mathcal{E}) \times GV_{soft} + b(\mathcal{E}). \tag{3}$$

In order to determine the functions at the left-hand side of Equations (2) and (3), we consider two fundamental relations:

- The mass attenuation coefficient of a chemical substance i with mass density ρ_i, $(\mu/\rho)_i$, is a function of its chemical composition, as is openly accessible from the NIST [36]; in particular, the mass attenuation coefficient of fat is directly given so that the mass density of fat ρ_{fat}=0.95 g/cm^3 [46] gives access to the attenuation coefficient of fat, as depicted by the black line in Figure 1.
- The X-ray attenuation coefficient of a composite material located inside one voxel is identical to the volume average of the X-ray attenuation coefficients of this material's single constituents [37–39]

$$\mu(\mathcal{E}) = \sum_{i=1}^{N_C} \mu_i(\mathcal{E}) \times f_i \tag{4}$$

with μ_i, $i = 1, ..., N_C$, as the X-ray attenuation coefficient of constituent i, N_C as the total number of constituents, and with f_i as the volume fraction of constituent i within the considered voxel.

Applying Equation (4) to the soft tissue, that is, inner organs and muscles localized around the spine, yields

$$\mu_{soft}(\mathcal{E}) = \mu_{H_2O}(\mathcal{E}) \times f_{H_2O} + \mu_{org}(\mathcal{E}) \times (1 - f_{H_2O}) \tag{5}$$

where the attenuation coefficient of water follows from its chemical formula H_2O; see second-lowest line in Figure 1, and that of organic material is approximated by the smallest amino acid, glycine (making up a high percentage of collagen, and being similar in structure to the remaining portion of collagen [48]), with chemical formula $C_2H_5NO_2$, see dotted line in Figure 1. The volume fraction of water, f_{H_2O}, is accessed through the average rule for the soft tissue mass density,

$$\rho_{soft} = f_{H_2O} \times \rho_{H_2O} + (1 - f_{H_2O}) \times \rho_{col}, \tag{6}$$

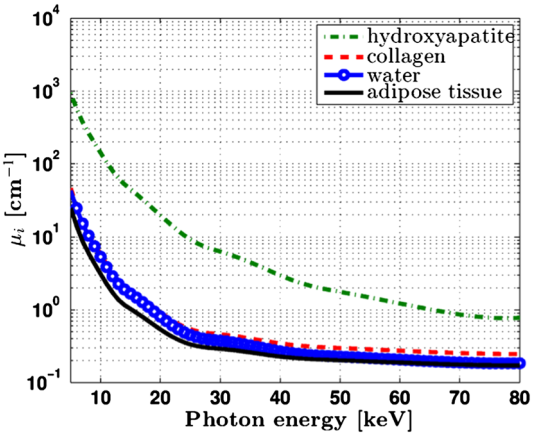

Figure 1. X-ray attenuation coefficients of the elementary constituents of bone tissue, and of adipose tissue; as functions of the photon energy (data reproduced from [36], in combination with the mass densities of adipose tissue [46], of collagen [47], and of hydroxyapatite [35]).

DOI: 10.1002/cnm

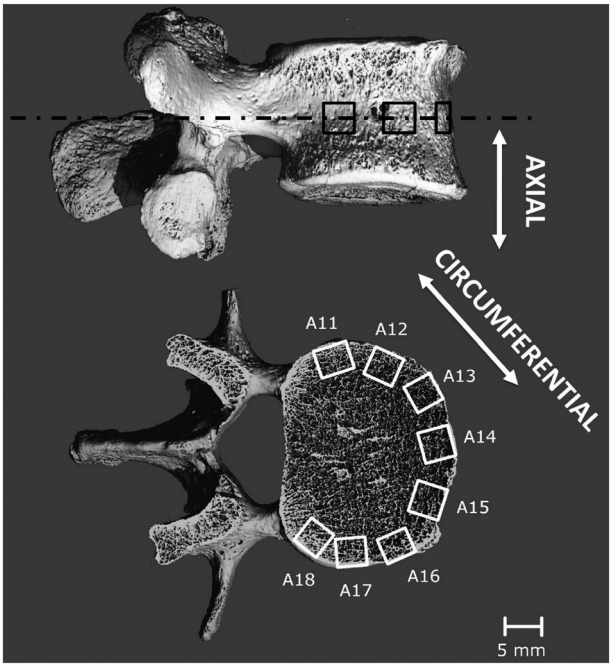

Figure 2. Micro computed tomography image of vertebra, adapted from Malandrino *et al*. (2012) [49], showing very thin "cortical shell", as well as original position and orientation of cubic samples cut from the investigated mid-height vertebra.

namely, through

$$f_{H_2O} = \frac{\rho_{soft} - \rho_{col}}{\rho_{H_2O} - \rho_{col}} \tag{7}$$

with the soft tissue mass density of tissues around the spine being documented as ρ_{soft}= 1.052 g/cm^3 [46] and ρ_{col}=1.42 g/cm^3 [47].

Conclusively, we solve Equations (2) and (3), while considering Equations (4)–(7), for $a(\mathcal{E})$ and $b(\mathcal{E})$.

2.2. *Identification of X-ray photon energy and of extracellular bone tissue mass density, based on general bone tissue composition rules*

As supplementary voxels of interest, we consider the densest voxel in the *corpus vertebrae*, GV_{max}, which hosts part of the 'cortical shell' of the vertebra. However, as seen from the microCT image of Figure 2, this shell is very thin, with a typical thickness of only 230 μm [50–52], so that the densest voxel (with a voxel size $l_{voxel} = 324$ μm) does not only contain cortical bone, but also adjacent vascular porosity or soft tissue around. Hence, we consider one additional voxel, namely, the densest neighbor of the voxel exhibiting GV_{max}, also containing both extravascular bone tissue resembling 'cortical bone', as well as vascular porosity or soft tissue, with GV_{soft}; see Figure 3.

The grey values related to the aforementioned two voxels are used for identification of the grey value GV_{ev}, which is related to a (fictitious) voxel being filled by extravascular bone tissue only. The aforementioned cortical shell thickness either lies fully within one single voxel, or it contributes to the attenuation coefficients of two neighboring voxels. In the latter case, the cortical shell thickness is partitioned between the two neighboring voxels, with voxel-specific parts l_1 and l_2, $l_1+l_2 = l_{cort}$; see Figure 3, and the former case can be seen as a limit of the latter, characterized by $l_2 = 0$ and $l_1 = l_{cort}$. The area of the voxel not covered by the cortical shell is considered as surrounding soft tissue on the exterior side of the vertebra, and gel-type, watery fluid-filled and soft cells-filled vascular pore space on the interior side. Because both materials exhibit very similar attenuation properties, we consider the same grey value for water and for soft tissue.

DOI: 10.1002/cnm

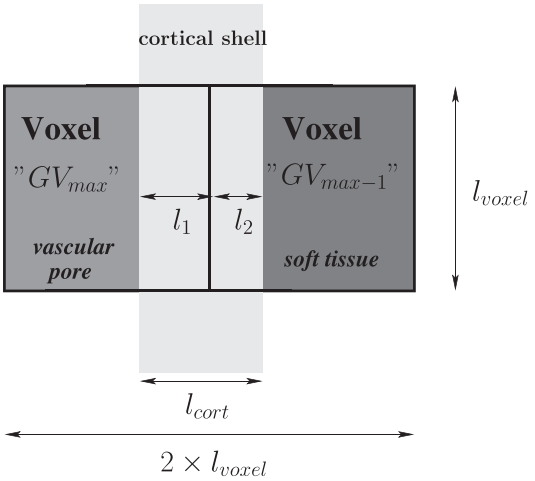

Figure 3. Partition of cortical shell (with thickness l_{cort}) between two neighboring voxels (with edge length l_{voxel}).

In order to use these partitioning considerations for identification of the *a priori* unknown grey value of the extravascular tissue, GV_{ev}, we use grey value-to-attenuation relation (1) in average rule (4), so as to show the existence of an average rule for the grey values as well,

$$GV = \sum_{i=1}^{N_C} GV_i \times f_i. \tag{8}$$

When applying (8) to the cortical shell partitioned between two voxels as depicted in Figure 3, one arrives at the following system of equations:

$$\frac{l_1}{l_{voxel}} \times GV_{ev} + \left(1 - \frac{l_1}{l_{voxel}}\right) \times GV_{soft} = GV_{max} \tag{9}$$

$$\frac{l_2}{l_{voxel}} \times GV_{ev} + \left(1 - \frac{l_2}{l_{voxel}}\right) \times GV_{soft} = GV_{max-1} \tag{10}$$

$$l_1 + l_2 = l_{cort}. \tag{11}$$

Solving these three equations for the unknowns GV_{ev}, l_1, and l_2, yields in particular the sought value for GV_{ev} as function of all the already identified grey values and length dimensions,

$$GV_{ev} = \frac{l_{voxel}}{l_{cort}} \times (GV_{max} + GV_{max-1} - 2GV_{soft}) + GV_{soft}. \tag{12}$$

In order to identify the X-ray energy $\mathcal{E}$, which then will allow for a unique scaling relation between grey values and attenuation coefficients, as given through Equation (1), we consider two independent ways to access the attenuation coefficient of the extravascular bone material, μ_{ev}. These two ways need to deliver *one single, unique result*:

- The first access to μ_{ev} is provided through

$$\mu_{ev}(\mathcal{E}) = a(\mathcal{E}) \times GV_{ev} + b(\mathcal{E}) \tag{13}$$

  fed with the energy-dependent proportionality constants derived from Equations (1)-(7).
- The second access is provided through repeated use of Equation (4) for upscaling attenuation coefficients from the level of the elementary constituents of bone tissue, up to the level of the extravascular bone material.

DOI: 10.1002/cnm

As regards the latter item, the NIST-data base allows for retrieval of the attenuation coefficients of the (mechanically relevant) elementary constituents of extracellular bone tissue: hydroxyapatite, organic material, and water. The two latter ones have been already introduced in Section 2.1, and the chemical formula $Ca_{10}(PO_4)_6(OH)_2$ allows for obtaining the hydroxyapatite-related attenuation curve, as depicted in Figure 1. Use of these functions in Equation (4), that is, upscaling from the elementary to the extracellular level, yields

$$\begin{aligned} \mu_{ec}^{up}(\mathcal{E}) =& \mu_{HA}(\mathcal{E}) \times f_{HA}^{ec} + \mu_{org}(\mathcal{E}) \times f_{org}^{ec} + \mu_{H_2O}(\mathcal{E}) \times f_{H_2O}^{ec} \\ & \text{with} \quad f_{H_2O}^{ec} + f_{org}^{ec} + f_{HA}^{ec} = 1. \end{aligned} \tag{14}$$

The constituent volume fractions f_{HA}^{ec}, f_{org}^{ec}, and $f_{H_2O}^{ec}$ (measured per volume of extracellular (ec) material) depend in a unique fashion on the tissue's extracellular mass density ρ_{ec}; see Figure 4, as evidenced in [30], from a multitude of weighing tests on dried, demineralized, deorganified, and ashed samples collected over 80 years of research [47, 53–63]. This implies the existence of a function $\mu_{ec}^{up}(\mathcal{E}, \rho_{ec})$, which can then be upscaled to the extravascular level through

$$\mu_{ev}^{up}(\mathcal{E}, \rho_{ec}) = \phi_{lac} \times \mu_{H_2O}(\mathcal{E}) + (1 - \phi_{lac}) \times \mu_{ec}^{up}(\mathcal{E}) \tag{15}$$

with the lacunar porosity ϕ_{lac}=0.10 [35, 64]. Expressions (13) and (15) need to deliver the same result, which we express as a ratio being equal to one,

$$\mu_{ev}(\mathcal{E}) / \mu_{ev}^{up}(\mathcal{E}, \rho_{ec}) = R(\mathcal{E}, \rho_{ec}) = 1. \tag{16}$$

Equation (16) defines a non-bijective function of the mass density as a function of the energy, that is, one energy value, more than one energy value, or no energy value, may be related to one and the same mass density value. From this function, the value for the extracellular mass density, which is related to only one, that is, unique, energy value, will be identified: this provides access to both the X-ray energy used for the image, and to the extracellular mass density of the investigated bone tissue from a human vertebra.

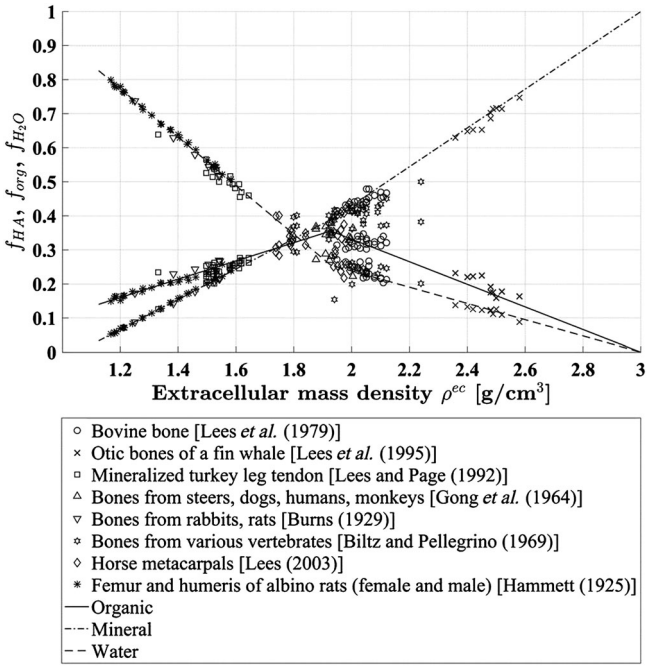

Figure 4. Universal composition rules in bone tissue [30]: bilinear relations between extracellular constituent volume fractions and tissue mass density.

DOI: 10.1002/cnm

2.3. Vertebra tissue mass density from weighing tests

In order to check the relevance of the value for the tissue mass density retrieved by means of the strategy outlined in Section 2.2, an independent experimental route towards ρ_{ec} is pursued, through the following protocol: From the mid-height portion of an elderly human vertebral body provided by the Medical University of Vienna, a slice was cut out by means of a band saw under continuous water irrigation (300 Cp; Exakt GmbH, Ingelheim, Germany). Out of this slice, eight cubes with 5–6 mm edge length were extracted by means of a wheel saw (Isomet, Buehler, USA). All the specimens had a face containing the external vertebral cortex, as can be seen in Figure 2. Two exactly parallel opposite surfaces orthogonal to the cortex layer were cut, whereby attention was paid on maintaining the cortex undamaged. Then, the specimens were immersed in an ultrasonic bath with 0.9% saline solution and standard soap, for 3 min at 40°C, in order to allow for mixing of the solution with the soap. Afterwards, the specimens were left in soaked state, during 24 hours at the same temperature for lipid dissolution. They were then washed with 0.9% saline solution for 10 min at 40°C under ultrasonic bath, and finally under flushing water at room temperature, in order to further clean the pores. The extracellular tissue density was measured by means of Archimedes' principle: The weight W_s of each specimen completely submerged in distilled water (air bubbles were removed under vacuum) was recorded by means of an analytical balance (PG403-S, Mettler-Toledo GmbH, Switzerland), as was the weight in air, W_a, the latter being accessible after centrifugation at 400 g for 15 min, in order to remove water from the vascular and lacunar pores. The mass density ρ_{ec} of the extracellular bone matrix was then determined according to

$$\rho_{ec} = \frac{W_a}{W_a - W_s}. \tag{17}$$

2.4. Voxel-specific tissue composition

Once the photon energy $\mathcal{E}$ is known, it gives access to the extravascular bone matrix attenuation coefficient via Equation (15), which can then be upscaled to the macroscopic bone material level: Therefore, we specify the average rule (4) for the constituents 'extravascular bone matrix' [with volume fraction (1-ϕ_{vas})] and vascular porosity (with volume fraction ϕ_{vas}), yielding

$$\mu_{macro} = \phi_{vas} \times \mu_{H_2O} + (1 - \phi_{vas}) \times \mu_{ev}. \tag{18}$$

Solving this equation for ϕ_{vas} gives access to voxel-specific values for the vascular porosity,

$$\phi_{vas} = \frac{\mu_{macro} - \mu_{ev}}{\mu_{H_2O} - \mu_{ev}}. \tag{19}$$

ϕ_{vas} can be also used to provide voxel-specific mass densities at the macroscopic scale

$$\rho_{macro} = \phi_{vas} \times \rho_{H_2O} + (1 - \phi_{vas}) \times \rho_{ev} \tag{20}$$

based on mass densities at the extravascular scale

$$\rho_{ev} = \phi_{lac} \times \rho_{H_2O} + (1 - \phi_{lac}) \times \rho_{ec} \tag{21}$$

Moreover, we are also interested in the apparent mass densities of mineral and collagen, that is, the 'bone mineral and collagen mass densities', the former one being sometimes referred to as vBMD [65].

Therefore, we convert the constituent volume fractions into apparent mass densities of hydroxyapatite, collagen, and water and non-collageneous proteins,

$$\rho_{HA}^{*,ec} = f_{HA}^{ec} \times \rho_{HA} \tag{22}$$

$$\rho_{col}^{*,ec} = 0.9 \times f_{org}^{ec} \times \rho_{col} \tag{23}$$

$$\rho_{H_2O+ncp}^{*,ec} = \rho_{ec} - \rho_{HA}^{*,ec} - \rho_{col}^{*,ec} \tag{24}$$

DOI: 10.1002/cnm

where we consider that 90% of the organic matter in extracellular bone matrix is collagen [66]. The apparent mass densities (22) – (24) are upscaled from the extracellular to the macroscopic level through

$$\begin{aligned}\rho^*_{HA} &= \rho^{*,ec}_{HA} \times (1-\phi_{lac}) \times (1-\phi_{vas}) \\ \rho^*_{col} &= \rho^{*,ec}_{col} \times (1-\phi_{lac}) \times (1-\phi_{vas}) \\ \rho^*_{H_2O+ncp} &= \rho_{macro} - \rho^*_{col} - \rho^*_{HA}\end{aligned} \tag{25}$$

2.5. *Intravoxel tissue elasticity*

The extracellular mass density and the spatial distribution of vascular porosities determined from a CT scan of a patient by means of a series of X-ray physics considerations, as described in Section 2.4 (see in particular Figure 11 for corresponding results), are now converted into voxel-specific elastic properties, on the basis of the multiscale homogenization scheme depicted in Figure 5.

This scheme, described in great detail in [29, 33, 35, 67], quantifies how the elementary mechanical constituents of bone, namely, hydroxyapatite, collagen, and water with some non-collageneous organics, as well as their dosages within the extracellular bone matrix, determine the elastic properties of bone at different length scales. It has been extensively validated experimentally, through an

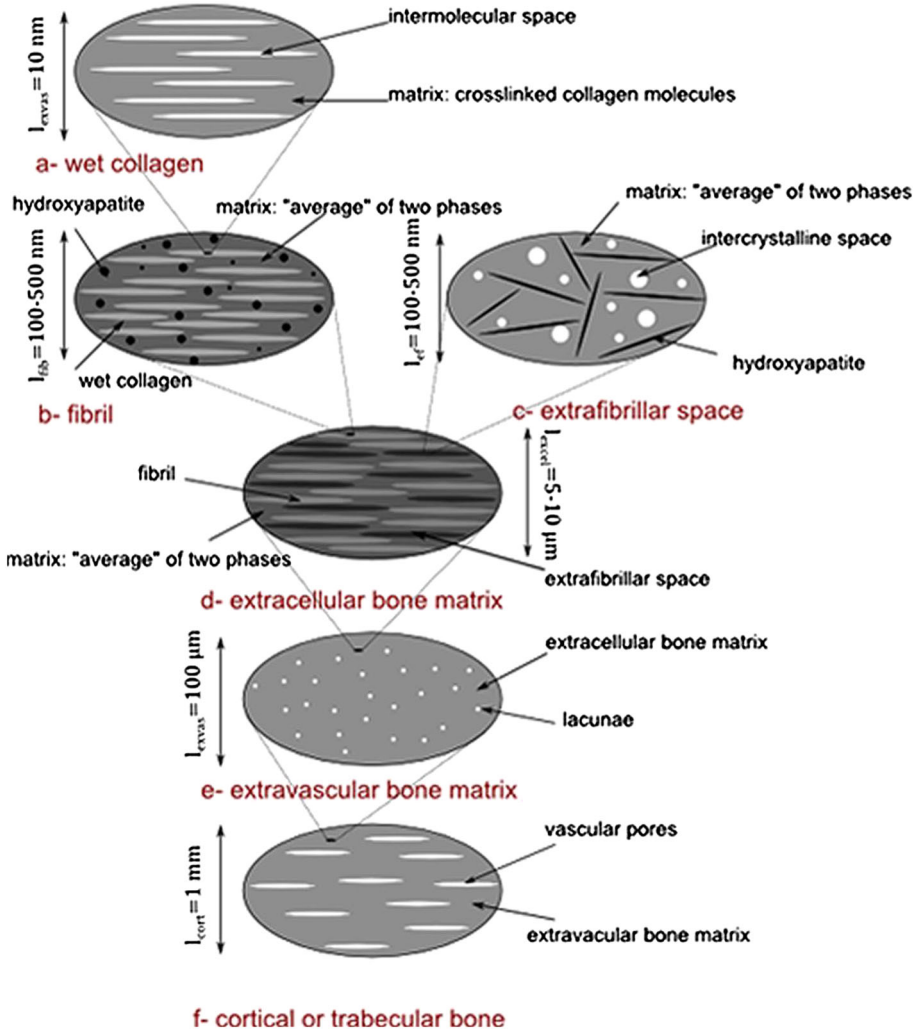

Figure 5. Multiscale micromechanical representation of bone material, according to Morin and Hellmich [35].

DOI: 10.1002/cnm

ultrasound database stemming from a wealth of bone sources – equine cortical bone [68], bovine tibia [53], drug-treated rabbit bone [69], whale malleus, incus, stapes, periotic and t. bulla [54], fin whale t. bulla [70], dugong rib, elephant radius, human femur, and deer antler [55] – in combination with 'universal'composition and mineralization rules for bone tissues [30–32, 71]. The latter were derived from a wealth of biophysical, biochemical, and biomechanical experimental sources [53, 56, 58–61, 72–80]. In this context, bone is represented by a series of representative volume elements (RVEs), the size of which is significantly larger than that of the inhomogeneities found within such a volume [e.g., Figure 5(f) with the vascular pores' diameters being scale-separated from the millimeter-size of the cortical or trabecular RVE]. Also, representation of the microstructure within the RVE is reduced to the bare minimum needed for elasticity homogenization: The domain within the RVE is subdivided into the minimum number of material phases with distinctively differing physical properties: their volume fractions [such as the vascular porosity in Figure 5(f)], their (average) elastic properties [such as those of the vascular pores and of the extravascular bone matrix in Figure 5(f)], the most fundamental shape characteristics (cylinders representing vascular pores in the case of cortical/trabecular bone), and their interaction [pore inclusions embedded into a solid matrix in Figure 5(f)]. This representation implies the following Mori–Tanaka-scheme-type expression for the stiffness of cortical/trabecular bone [37],

$$\begin{aligned}\mathbb{C}_{macro} =& \left\{\phi_{vas}\mathbb{C}_{H_2O} : [\mathbb{I} + \mathbb{P}_{cyl} : (\mathbb{C}_{H_2O} - \mathbb{C}_{ev})]^{-1} + (1-\phi_{vas})\mathbb{C}_{ev}\right\} : \\ & : \left\{\phi_{vas}[\mathbb{I} + \mathbb{P}_{cyl} : (\mathbb{C}_{H_2O} - \mathbb{C}_{ev})]^{-1} + (1-\phi_{vas})\mathbb{I}\right\}^{-1}\end{aligned} \tag{26}$$

with ϕ_{vas} as the vascular porosity, $\mathbb{C}_{ev}$ and $\mathbb{C}_{H_2O}$ as the elastic stiffness of the extravascular bone matrix and of water, $\mathbb{I}$ as the fourth-order identity tensor with components $I_{ijkl} = \frac{1}{2}(\delta_{ik}\delta_{jl} + \delta_{il}\delta_{jk})$, with the Kronecker delta δ_{ij} being equal to 1 for $i = j$ and zero otherwise, and $\mathbb{P}_{cyl}$ as the fourth-order Hill tensor accounting for the cylindrical shape of the inclusions embedded into a transversely isotropic matrix with stiffness $\mathbb{C}_{ev}$ [67].

Within the investigated vertebral body, the vascular porosity is varying from voxel to voxel, as depicted in Figure 11; all other quantities in Equation (26) are constant. Particularly, the extravascular stiffness follows from feeding the homogenization scheme of Figure 5 with an extracellular mass density resulting from Equation (16) (and corresponding extracellular volume fractions of mineral, collagen, and water as given in Figure 12), as well as with a lacunar porosity of 10 % [35, 64].

The stiffness tensor of water reads as $\mathbb{C}_{H_20} = 3\mathbb{I}_{vol}k_{H_20}$, with the bulk modulus of water amounting to k_{H_2O}=2.3 GPa [81], and with $\mathbb{I}_{vol}$ as the volumetric part of the fourth-order identity tensor, with components $I_{vol,ijkl} = \frac{1}{3}\delta_{ij}\delta_{kl}$.

2.6. Linear finite element simulations

The used finite element model is based on earlier work published in [82]; see Figure 6. It consists of 125,253 solid elements representing the trabecular bone tissue, and 17,185 shell elements representing the cortical bone tissue. For the present study, we realized a cortical shell thickness of l_{cort}=0.23 mm [50–52], while the caudal and cranial (bony) endplates were assigned thicknesses of l_{end} = 1 mm [83, 84]. In order to investigate the effect of heterogeneity at the finite element level (i.e., with gradients measured along a few millimeters), we considered two ways of assigning material properties to the finite element model of Figure 6:

- For the so-called 'homogeneous model', the entire trabecular bone compartment is assigned the same elastic stiffness tensor, namely, that related to the average vascular porosity found in that compartment, ϕ_{vas}^{trab}= 0.86. More precisely, given the 'short-beam'-type nature of our structure, we assign the longitudinal Young's modulus

$$E_{macro,3} = \frac{1}{C^{-1}_{macro,3333}} = 1322 \text{ MPa} \tag{27}$$

DOI: 10.1002/cnm

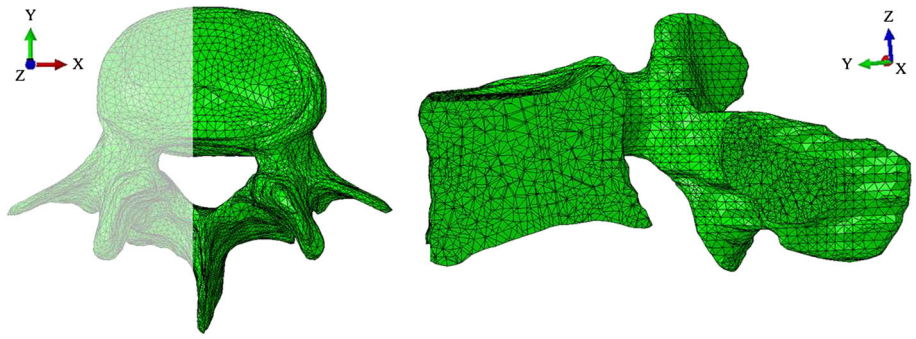

Figure 6. Finite element mesh of the patient-specific vertebral body.

with $C^{-1}_{macro,3333}$ as the longitudinal normal component of the compliance tensor $\mathbb{C}^{-1}_{macro}$ and the longitudinal Poisson's ratio

$$\nu_{31} = -C^{-1}_{macro,1133} \times E_{macro,3} = 0.19 \tag{28}$$

as 'formally isotropic' material properties to the finite element model, as is normally considered as an appropriate approximation in bone organ mechanics [43, 85, 86]. As regards the very thin cortical shell around the organ whose thickness of 230 μm does not quite allow for accommodation of Haversian systems (and hence of the vascular porosity), we adopt the 'macroscopic' stiffness tensor $\mathbb{C}_{macro}$ related to zero-porosity, that is, that of the extravascular bone matrix according to Equation (48). More precisely, as before, we assign as formally isotropic properties, a Young's modulus and a Poisson's ratio of 9406 MPa and of 0.28, respectively, to the shell finite elements.

- For the "heterogeneous model", the cortical shell treatment does not differ, while the element-specific stiffness tensors are computed from the vascular porosity values assigned to the centroids of the finite elements. The interpolation between the CT data and the finite elements is made by finding the three CT voxels which are closest to the element centroid. The porosity values related to these three voxels are then averaged and assigned to the finite element.

Because the focus of the present study is on the effect of material properties rather than on different loading conditions, we consider a very basic load case, related to mild physiological activity: A pressure amounting to 1 MPa is applied to the cranial endplate, while the caudal endplate is pinned in all space directions. The pressure magnitude is indeed related to 'quasi-physiological conditions': half of the body weight of a person of 65-kg mass in the gravitational field of the earth would results in a pressure of 0.55 MPa, when evenly distributed across the surface area A_{end}= 571 mm^2 of the cranial endplate. This would be the "static deadload", about half of the value prescribed to account for mild physiological activity.

In order to test the robustness of our model, we compare the computational results of four models with increasing element sizes, that is, decreasing amount of elements, namely, 229,138, 143,159, 105,763, and 82,848 elements. More precisely, we compute, for all element sizes, the strain energy density ψ_n in the n-th finite element as follows:

$$\psi_n = \frac{1}{2}\boldsymbol{\varepsilon}_n : \mathbb{C}_{macro,n} : \boldsymbol{\varepsilon}_n \tag{29}$$

with $\boldsymbol{\varepsilon}_n$ denoting the macroscopic strains in element n, so that the average strain energy over the entire organ reads as follows:

$$\overline{\psi}_{organ} = \frac{1}{V_{organ}} \sum_{n=1}^{N_n} \psi_n \times V_n \tag{30}$$

with N_n as the number of finite elements, with V_n as the volume of the n-th finite element and V_{organ} as the volume of the entire organ. The results of the linear elastic finite element simulations are then used for safety assessment of the investigated structure. More precisely, we check by which

DOI: 10.1002/cnm

proportionality factor the determined element-specific macroscopic stresses needed to be increased, so as to reach ultimate macroscopic bone material failure. This stress increase, however, is subjected to macroscopic bone RVEs in an incremental fashion, allowing for elastoplastic deformation states prior to the ultimate material failure (which obviously depends on these elastoplastic deformations). In order to quantify them, we extend the hierarchical scheme depicted in Figure 5 to the realm of elastoplasticity, extending earlier work published in [34]. There, the liquid crystal-type water interfaces between the mineral crystals and/or crystal clusters in the extrafibrillar space [see Figure 5(c)] have been identified as the major nanoscopic origin of bone elastoplasticity, both from the high interaction energies between water and hydroxyapatite as evidenced by several molecular dynamics and nuclear magnetic resonance studies [87–91], and more importantly, by successfully predicting, based on experimentally obtained upscaling mineral and collagen strengths [92–94], the macroscopic strengths of different types of bone [95–112]. Such successful representations of bone microstructure for mechanical property predictions, which do not resolve the material up to the highest resolution ever possible, but rather focus on reliable consideration of the mechanically most important micromorphological features, have not only been developed in the framework of continuum micromechanics or random homogenization theory, but also in alternative theoretical frames, such as that of lattice models [113].

In the present case, however, fluid-induced, mutual sliding of crystals is associated to elastoplastic hydroxyapatite mineral phases, which are oriented uniformly in all space directions, as given through Eulerian angles ϕ and θ related to spherical coordinates. These phases obey the following constitutive equations. The needle-shaped mineral phase oriented in space direction (ϕ, θ) follows an elastoplastic stress–strain relation,

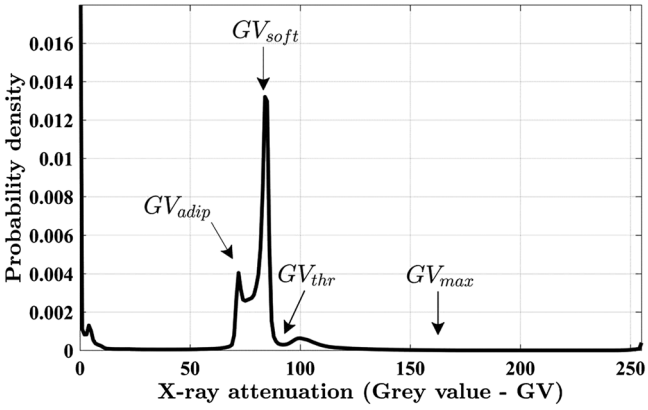

Figure 7. Frequency distribution plot of the attenuation information in terms of grey values of the vertebral body L3.

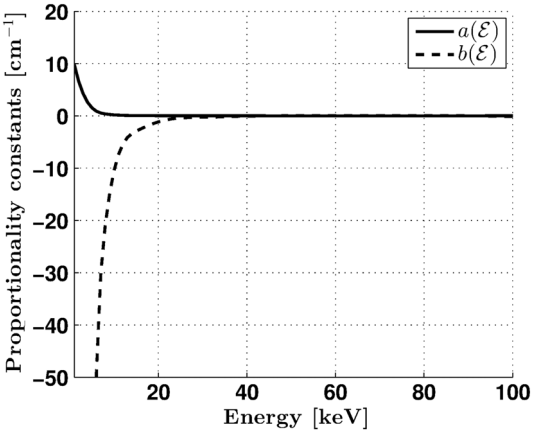

Figure 8. Slope and intercept parameters a and b, as functions of the photon energy $\mathcal{E}$.

DOI: 10.1002/cnm

$$\boldsymbol{\sigma}_{HA,\phi\theta} = \mathbb{C}_{HA} : \left(\boldsymbol{\varepsilon}_{HA,\phi\theta} - \boldsymbol{\varepsilon}^{p}_{HA,\phi\theta}\right) \tag{31}$$

with $\mathbb{C}_{HA} = 3k_{HA}\mathbb{I}_{vol} + 2G_{HA}\mathbb{I}_{dev}$ as the isotropic elasticity of hydroxyapatite, k_{HA}= 82.6 GPa and G_{HA}= 44.9 GPa [114], $\mathbb{I}_{dev} = \mathbb{I} - \mathbb{I}_{vol}$ as the deviatoric component of the fourth-order identity tensor, $\boldsymbol{\varepsilon}_{HA,\phi\theta}$ and $\boldsymbol{\varepsilon}^{p}_{HA,\phi\theta}$ as the (average) total and plastic strains in the $(\phi\theta)$-oriented needle-shaped phase, and $\boldsymbol{\sigma}_{HA,\phi\theta}$ as the corresponding average stress. Plastic events are quantified by means of a Mohr–Coulomb criterion,

$$\mathcal{F}_{HA,\phi\theta} = \mathcal{F}(\boldsymbol{\sigma}_{HA,\phi\theta}) = \beta\sigma^{I}_{HA,\phi\theta} - \sigma^{III}_{HA,\phi\theta} - \sigma^{y}_{HA} \leqslant 0 \tag{32}$$

with β as the ratio between the compressive and the tensile yield stresses ($\beta = 12$), σ^{y}_{HA} as the compressive yield stress (σ^{y}_{HA}=570 MPa), and $\sigma^{I}_{HA,\phi\theta} \geqslant \sigma^{II}_{HA,\phi\theta} \geqslant \sigma^{III}_{HA,\phi\theta}$ as the (sorted) principal stresses in the $(\phi\theta)$-oriented mineral phase. The strength parameters follow from tests on porous hydroxyapatite polycrystals [115–123], mimicking those occurring in the extrafibrillar space of Figure 5(c). Potential occurence of plastic events follows the Kuhn–Tucker conditions [124] (actually proposed already in 1938 by Melan [125])

$$\dot{\lambda}_{HA,\phi\theta} \geqslant 0, \quad \mathcal{F}_{HA,\phi\theta} \leqslant 0 \quad \text{and} \quad \dot{\lambda}_{HA,\phi\theta} \times \mathcal{F}_{HA,\phi\theta} = 0 \tag{33}$$

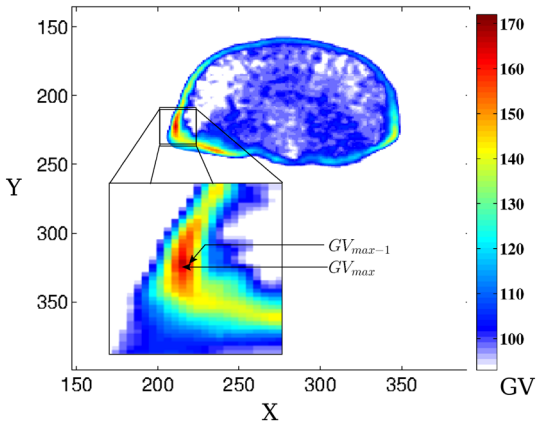

Figure 9. Grey value distribution throughout vertebral cross section where the densest voxel (with GV_{max}) and its neighbor (with GV_{max-1}) occur.

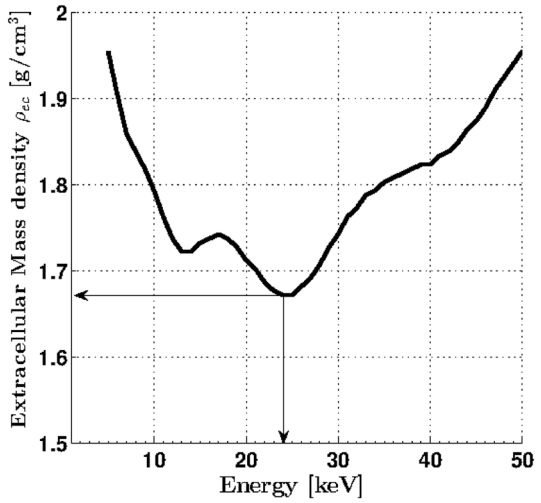

Figure 10. Extracellular mass density as function of photon energy, according to Equations (1)–(20), with $a(\mathcal{E})$ and $b(\mathcal{E})$ as depicted in Figure 8.

DOI: 10.1002/cnm

in conjunction with the following, non-associative, isochoric flow rule:

$$\dot{\boldsymbol{\varepsilon}}^{p}_{HA,\phi\theta} = \dot{\lambda}_{HA} \frac{\partial \mathcal{G}}{\partial \boldsymbol{\sigma}_{HA,\phi\theta}} \qquad \text{with} \qquad \mathcal{G}(\boldsymbol{\sigma}_{HA,\phi\theta}) = \sigma^{I}_{HA,\phi\theta} - \sigma^{III}_{HA,\phi\theta}, \tag{34}$$

whereby the dot denotes the time derivative, $\mathcal{G}$ denotes the flow potential, the derivative of which accounts for the plastic flow direction, and $\dot{\lambda}_{HA,\phi\theta}$ denotes the plastic multiplier quantifying the amount of plastic strain.

Such plastic events imply more and more micro-stresses to be transferred to the molecular collagen of Figure 5(a), which finally fails in a brittle manner, according to a Rankine-type criterion,

$$\mathcal{F}_{col} = \max_{i \in \{I,II,III\}} |\sigma^{i}_{col}| - \sigma^{ult}_{col} \leqslant 0 \tag{35}$$

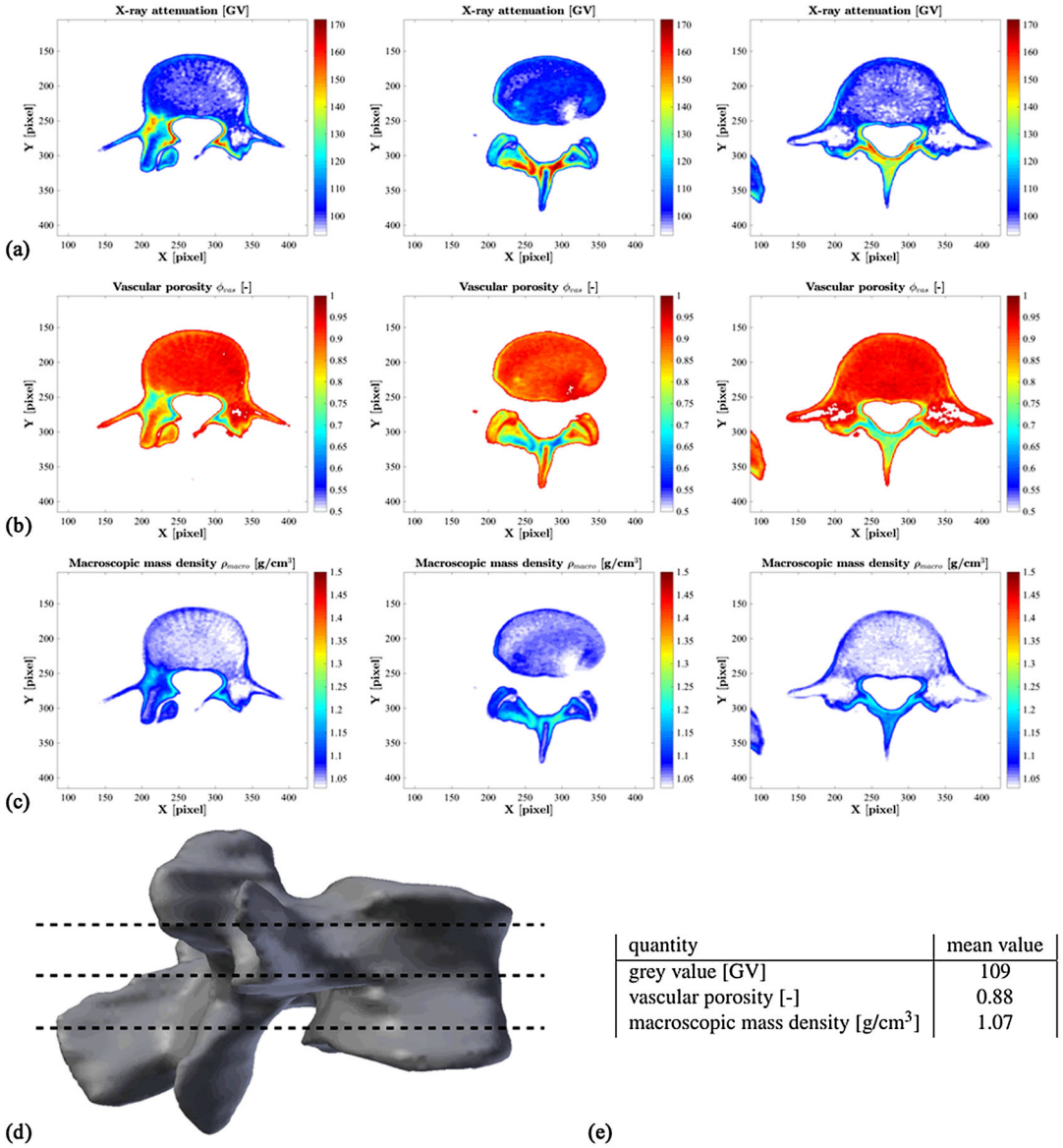

quantity	mean value
grey value [GV]	109
vascular porosity [-]	0.88
macroscopic mass density [g/cm^3]	1.07

Figure 11. Property maps in computed tomography slices in the transverse plane: (a) X-ray attenuation coefficient in terms of grey value, (b) vascular porosity, (c) macroscopic mass density, (d) locations of the mapped cross sections, and (e) mean values of the previous quantities.

DOI: 10.1002/cnm

with $\sigma^{i}_{col}, i = I...III$, as the eigenstresses in the molecular collagen assembly at the wet collagen (microfibrillar) scale (i.e. the matrix made up by crosslinked collagen molecules shown in Figure 5), and σ^{ult}_{col} as the strength of molecular collagen. The latter quantity is derived from experiments on rat tail tendon, which, under wet conditions, exhibits a strength of 106.1 MPa [94]. We consider close packing of collagen, so as to obtain access to the properties of molecular collagen. It is known from neutron diffraction studies [47, 76] that diffractional spacing (a measure for the lateral distance of collagen molecules) reduces from 1.52 nm (for wet collagen) to 1.09 nm [for maximally packed (dry) collagen]. Accordingly, the cross-sectional area of a tensile specimen would reduce by the ratio $(1.52/1.09)^2$, so that the strength of molecular collagen follows to be $(1.52/1.09)^2$ times higher than that of wet collagen, that is, 206 MPa.

These elastoplastic and failure laws need to be homogenized over the RVEs depicted in Figure 5, so as to determine the elastoplastic behavior of a piece of cortical/trabecular bone illustrated in Figure 5(f). This is achieved in the framework of continuum micromechanics [126] by means of

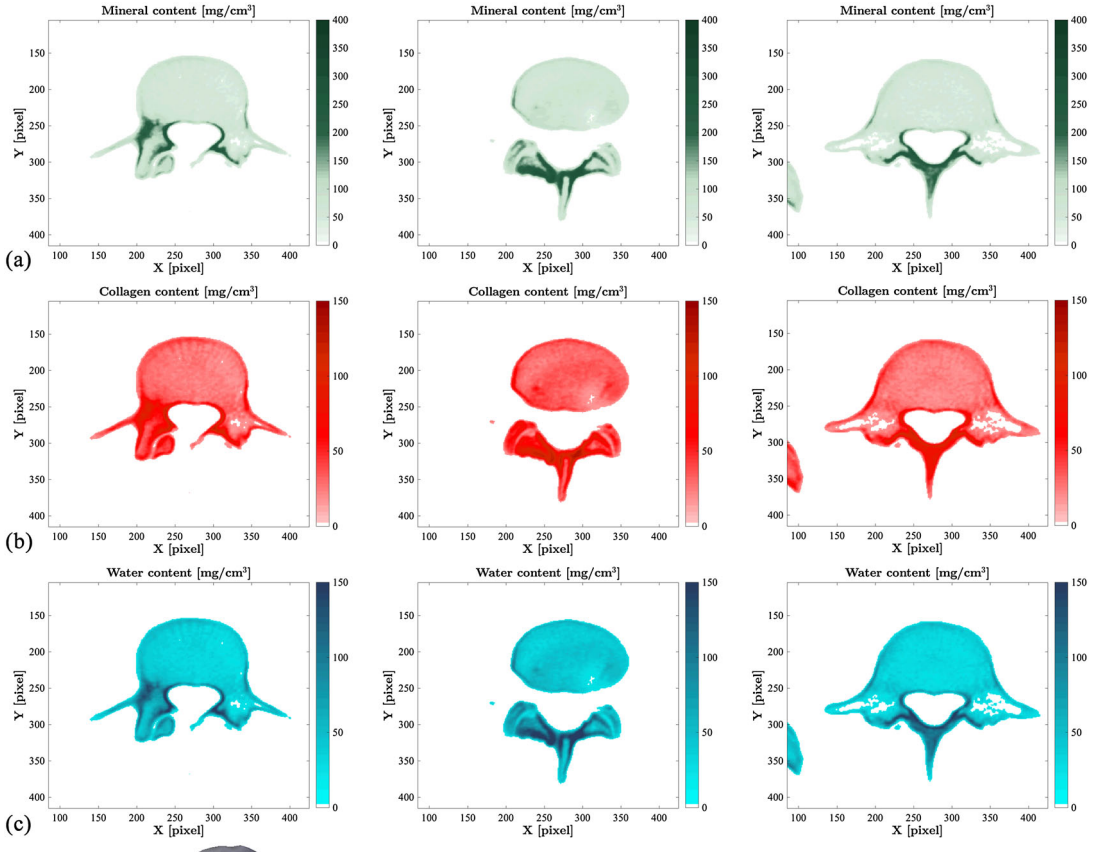

quantity	mean value [mg/cm³]
mineral content	87.8
collagen content	39.2
water + ncp content	944

Figure 12. Property maps in computed tomography slice in the transverse plane: (a) Mineral content, (b) collagen content, (c) water and non-collageneous proteins (ncp) content, (d) locations of the mapped cross sections, and (e) mean values of the previous quantities.

DOI: 10.1002/cnm

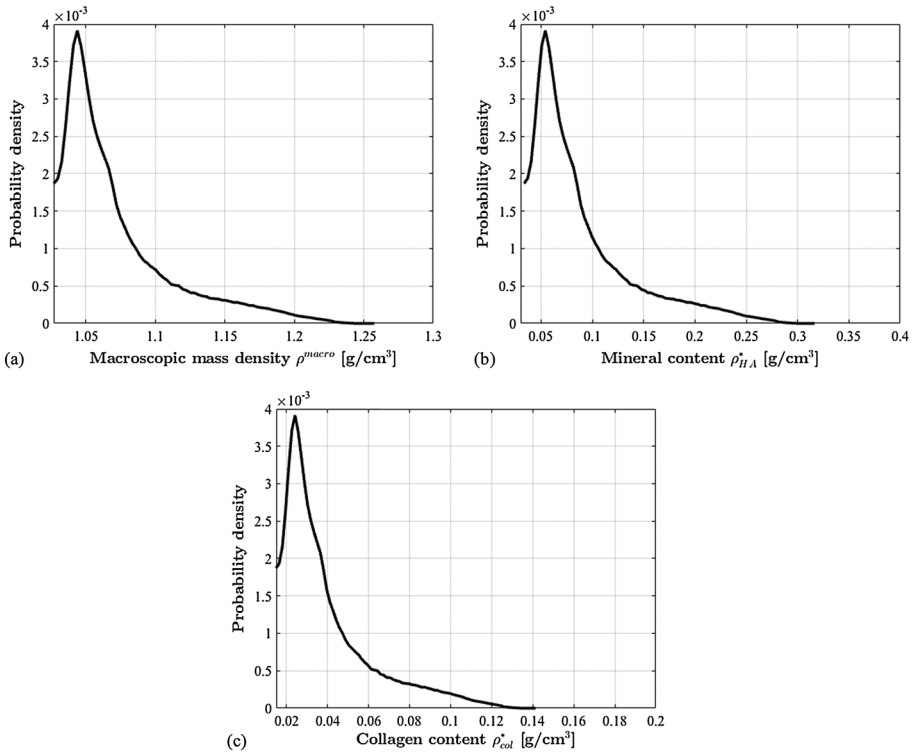

Figure 13. Probability density plots of (a) the macroscopic mass density, (b) the mineral content, and (c) the collagen content.

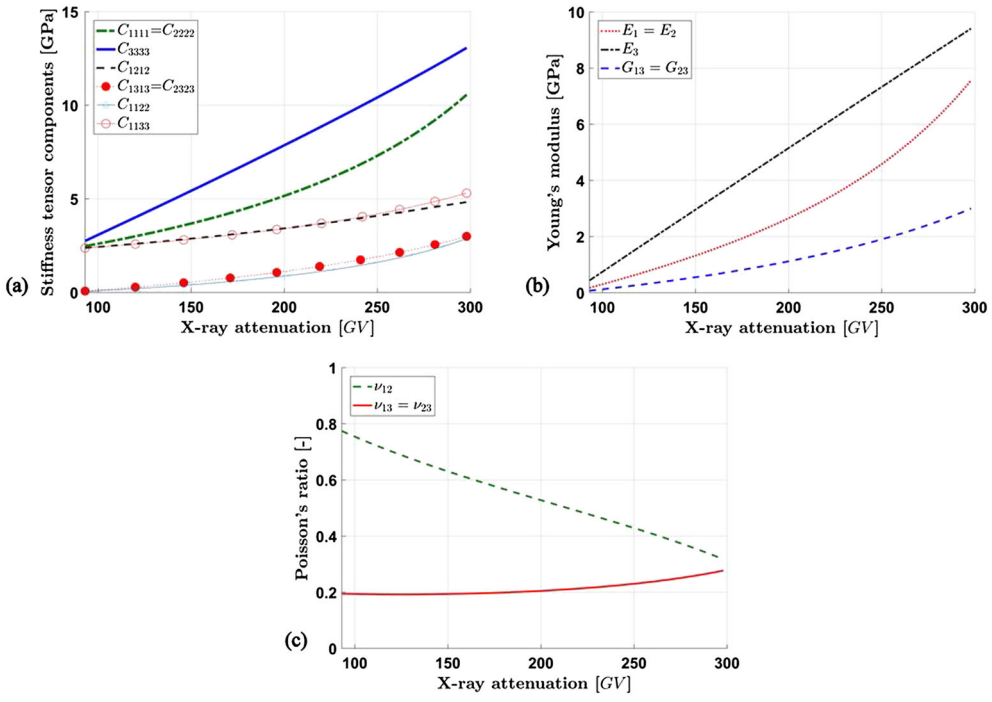

Figure 14. Translation of X-ray attenuation information into bone elasticity at the voxel scale: (a) stiffness tensor components, (b) Young's and shear moduli, and (c) Poisson's ratios; 1,2 ... transverse direction, 3 ... axial direction.

DOI: 10.1002/cnm

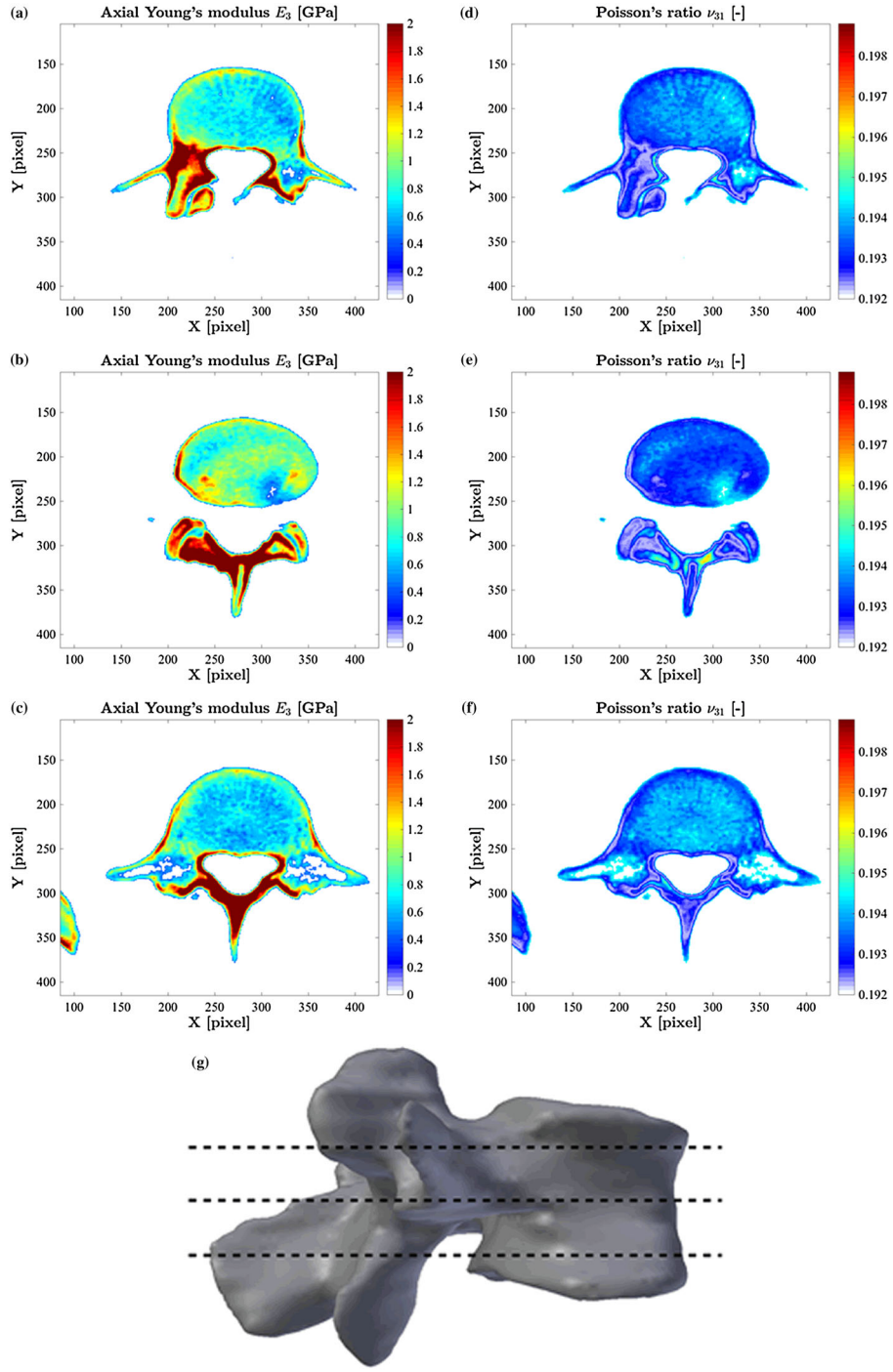

Figure 15. Property maps in computed tomography slices in the transverse plane: (a–c) axial Young's modulus, and (d–f) axial Poisson's ratio; (g) locations of the mapped cross sections.

stress and strain averaging rules [127, 128] and concentration-influence relations [129], applied to each of the RVEs depicted in Figure 5. As regards the extrafibrillar RVE, homogeneous strains $\mathbf{E}_{ef}$ are prescribed in terms of displacements

$$\boldsymbol{\xi}(\mathbf{x}) = \mathbf{E}_{ef} \cdot \mathbf{x} \tag{36}$$

DOI: 10.1002/cnm

at the boundary of the RVE – $\mathbf{x}$ is the "microscopic" location vector with a resolution much smaller than the RVE. This boundary condition implies that kinematically compatible microstrains $\boldsymbol{\varepsilon}(\mathbf{x})$

$$\boldsymbol{\varepsilon}(\mathbf{x}) = \nabla^s \boldsymbol{\xi}(\mathbf{x}) \tag{37}$$

fulfill the following strain average rule [115, 126]

$$\mathbf{E}_{ef} = f_{HA}^{ef} \int_{\phi=0}^{2\pi} \int_{\theta=0}^{\pi} \boldsymbol{\varepsilon}_{HA,\phi\theta} \frac{\sin\theta}{4\pi} d\phi d\theta + \left(1 - f_{HA}^{ef}\right) \boldsymbol{\varepsilon}_{ic} \tag{38}$$

with f_{HA}^{ef} as the volume fraction of hydroxyapatite within the extrafibrillar RVE and $\boldsymbol{\varepsilon}_{ic}$ as the (average) strains in the inter-crystalline space. Moreover, when applying the principle of virtual powers to this RVE, resulting in the so-called Hill's lemma [126], one arrives at the stress average rule for the macroscopic stresses Σ_{ef} acting on the extrafibrillar RVE,

$$\boldsymbol{\Sigma}_{ef} = f_{HA}^{ef} \int_{\phi} \int_{\theta} \boldsymbol{\sigma}_{HA,\phi\theta} \frac{\sin\theta}{4\pi} d\phi d\theta + \left(1 - f_{HA}^{ef}\right) \boldsymbol{\sigma}_{ic} \tag{39}$$

with the microstresses $\boldsymbol{\sigma}(\mathbf{x})$ fulfilling the equilibrium condition

$$\operatorname{div} \boldsymbol{\sigma}(\mathbf{x}) = 0. \tag{40}$$

Linearity of Equations (40), (37), (36), and (31) implies the strains in the $(\phi\theta)$-oriented mineral phase to depend multi-linearly on the homogeneous strains $\mathbf{E}_{ef}$ and on the plastic (micro-)strains $\boldsymbol{\varepsilon}_{HA,\phi\theta}^{p}$ found in all mineral phases,

$$\boldsymbol{\varepsilon}_{HA,\phi\theta} = \mathbb{A}_{HA,\phi\theta} : \mathbf{E}_{ef} + \int_{\Phi} \int_{\Theta} \mathbb{D}_{\phi\theta\Phi\Theta} : \boldsymbol{\varepsilon}_{HA,\Phi\Theta}^{p} \frac{\sin\Theta}{4\pi} d\Phi d\Theta. \tag{41}$$

Similarly, the microstrains $\boldsymbol{\varepsilon}_{ic}$ found in the inter-crystalline pores read as follows:

$$\boldsymbol{\varepsilon}_{ic} = \mathbb{A}_{ic} : \mathbf{E}_{ef} + \int_{\Phi} \int_{\Theta} \mathbb{D}_{ic,\Phi\Theta} : \boldsymbol{\varepsilon}_{HA,\Phi\Theta}^{p} \frac{\sin\Theta}{4\pi} d\Phi d\Theta \tag{42}$$

with $\mathbb{A}_{HA,\phi\theta}$ and $\mathbb{A}_{ic}$ as the concentration tensors of the hydroxyapatite phase oriented in direction $(\phi\theta)$ and of the inter-crystalline phase, respectively, and $\mathbb{D}_{\phi\theta\Phi\Theta}$ and $\mathbb{D}_{ic,\Phi\Theta}$ accounting for the influence of plastic strains occurring in the $(\Phi\Theta)$-oriented phase, on the total strains occurring in the mineral phase oriented in $(\phi\theta)$-direction and in the inter-crystalline phase, respectively. These concentration and influence tensors are derived from extended 'eigenstressed' Eshelby problems [126], as given in more detail in [130, 131]. Finally, repeated use of Hill's lemma yields the upscaled 'macroscopic' elastoplastic constitutive equation as follows:

$$\boldsymbol{\Sigma}_{ef} = \mathbb{C}_{ef} : \left(\mathbf{E}_{ef} - \mathbf{E}_{ef}^{p}\right) \tag{43}$$

where $\mathbb{C}_{ef}$ is the homogenized stiffness tensor of the extrafibrillar space, reading as follows:

$$\mathbb{C}_{ef} = f_{HA}^{ef} \mathbb{C}_{HA} : \int_{\theta} \int_{\phi} \mathbb{A}_{HA,\phi\theta} \frac{\sin\theta}{4\pi} d\phi d\theta + \left(1 - f_{HA}^{ef}\right) \mathbb{C}_{H_2O} : \mathbb{A}_{ic} \tag{44}$$

DOI: 10.1002/cnm

and the extrafibrillar plastic strains $\mathbf{E}^{p}_{ef}$ fulfill

$$\mathbf{E}^{p}_{ef} = \mathbb{C}^{-1}_{ef} : f^{ef}_{HA} \int_{\phi} \int_{\theta} {}^{t}\mathbb{A}_{HA,\phi\theta} : \mathbb{C}_{HA} : \boldsymbol{\varepsilon}^{p}_{HA,\phi\theta} \frac{\sin\theta}{4\pi} d\phi d\theta, \tag{45}$$

whereby the superscript t denotes the transpose of the concentration tensor (${}^{t}A_{ijkl} = A_{klij}$). Equations (31)–(45) allow one to determine the plastic events in the crystal phases caused by extrafibrillar loading – once Equations (38), (39), (41), (42), (44), (45) are discretized in space, here by means of the numerical scheme proposed in [132], and Equations (33) and (34) are discretized in (chronological) time, here by means of the return mapping algorithm [124, 133]. In particular, the multisurface plasticity concept is realized for Mohr–Coulomb plasticity [134]. This is carried out for all RVEs depicted in Figure 5, so as to relate macroscopic loading at the level of cortical/trabecular bone, to plastic strains in the crystalline, extrafibrillar, extracellular, and extravascular phases in Figure 5, until the molecular collagen stresses fulfill failure criterion (35).

Within this theoretical framework, two types of 'safety factors', 'loading degrees', or 'distances to failure' are determined:

- The macroscopic trabecular bone-related stresses $\boldsymbol{\Sigma}_{macro}$ determined in each finite element are first multiplied with a factor χ_y related to just reaching the yield limit defined by equality in Equation (32);

$$\boldsymbol{\Sigma}_{macro,y} = \chi_y \boldsymbol{\Sigma}_{macro}. \tag{46}$$

  This factor is called the yield safety factor; it is larger than one for elastic deformation states and reduces to one once yielding starts. Its inverse is the 'yield loading degree' or 'distance to yielding', being smaller than one for elastic deformation states, and increasing towards one when approaching yielding states.
- Secondly, the aforementioned element-specific macroscopic stresses are multiplied with a factor χ_{ult} related to reaching the ultimate load defined by equality in Equation (35);

$$\boldsymbol{\Sigma}_{macro,ult} = \chi_{ult} \boldsymbol{\Sigma}_{macro}. \tag{47}$$

  This factor is called the (local, material-based) ultimate safety factor; it is larger than one for deformation states, which the macroscopic bone material can still withstand and reduces to one once the material fails (through collagen tearing). Its inverse is the 'ultimate loading degree'or 'distance to failure', being smaller than one for bearable deformation states, and increasing towards one when approaching material failure.

3. RESULTS

Evaluation of all grey values found in the investigated clinical CT image in form of the normalized histogram or probability density function depicted in Figure 7 allows for identification of the anatomical landmark values related to adipose tissue, as $GV_{fat} = 72$, to soft tissues from inner organs, as $GV_{soft} = 84$, and to bone tissue, as $GV_{bone} = 101$; see Figure 7. In addition, the histogram provides the segmentation threshold as $GV_{thr} = 93$. From the landmark grey values for the fat and soft tissues, Equations (1) to (7) allow for identification of the energy-dependent slope and intercept parameters a and b; see Figure 8. They allow for (still X-ray energy-dependent) conversion of grey values to the actual physical quantities they represent.

As illustrated in Figure 9, the maximum grey value occurring in the *corpus vertebrae* amounts to $GV_{max} = 164$, and its densest neighbor exhibits a grey value of $GV_{max-1} = 156$. According to Equation (12), this allows for identification of the grey value related to extravascular bone as $GV_{ev} = 298$.

A unique relation between grey values and X-ray attenuation coefficients can be only obtained for an extracellular mass density of 1.67 g/cm^3, being assigned to an X-ray energy of 24 keV, as is evident from Figure 10, drawn on the basis of Equations (13) to (16). This mass density agrees very well with the one measured by Archimedes' principle as determined in Section 2.3; the

DOI: 10.1002/cnm

latter amounting to 1.71±0.11 g/cm^3 (mean value ± standard deviation). Use of ρ_{ec}=1.67 g/cm^3 and of corresponding extracellular volume fractions of hydroxyapatite f_{HA}=0.27, organic matter f_{org}=0.29, and water f_{H_2O}=0.44 in the homogenization scheme of Figure 5 yields the extravascular stiffness tensor

$$\mathbb{C}_{ev} = \begin{pmatrix} C_{1111} & C_{1122} & C_{1133} & 0 & 0 & 0 \\ C_{1122} & C_{2222} & C_{2233} & 0 & 0 & 0 \\ C_{1133} & C_{2233} & C_{3333} & 0 & 0 & 0 \\ 0 & 0 & 0 & 2C_{2323} & 0 & 0 \\ 0 & 0 & 0 & 0 & 2C_{1313} & 0 \\ 0 & 0 & 0 & 0 & 0 & 2C_{1212} \end{pmatrix} = \\ = \begin{pmatrix} 10.56 & 4.82 & 5.30 & 0 & 0 & 0 \\ 4.82 & 10.56 & 5.30 & 0 & 0 & 0 \\ 5.30 & 5.30 & 13.06 & 0 & 0 & 0 \\ 0 & 0 & 0 & 5.99 & 0 & 0 \\ 0 & 0 & 0 & 0 & 5.99 & 0 \\ 0 & 0 & 0 & 0 & 0 & 5.75 \end{pmatrix} \text{ in GPa.} \tag{48}$$

Evaluation of the energy-dependent functions of Figure 8 for the photon energy as 24 keV yields the grey value-to-attenuation conversion factors a and b as $a = 0.0107$ cm^{-1} and $b = -0.4154$ cm^{-1}. Evaluation of relations (20) and (25) for the grey value of each and every voxel of the scanned object yields density and hydroxyapatite/collagen/water content maps throughout the vertebral body; see Figure 11 and 12, as well as frequency plots of the aforementioned quantities, Figure 13.

The expected (i.e., most frequently occurring) values for macroscopic mass density, mineral, and collagen content amount to $\rho_{macro}^{EV} = 1.04$ g/cm^3, $\rho_{HA}^{*,EV} = 54.1$ mg/cm^3, and $\rho_{col}^{*,EV} = 39.1$ mg/cm^3, while their averages over the entire vertebral body amount to $\overline{\rho_{macro}} = 1.07$ g/cm^3, $\overline{\rho_{HA}^{*}} = 87.8$ mg/cm^3, and $\overline{\rho_{col}^{*}} = 39.2$ mg/cm^3.

The micromechanics-based porosity-stiffness relations based on the hierarchical representation depicted in Figure 5; see also Equations (26) and (48), in combination with the X-ray physics-based grey value-to-porosity conversion scheme described in Section 2.4, yields organ-specific grey value-to-stiffness relations as depicted in Figure 14.

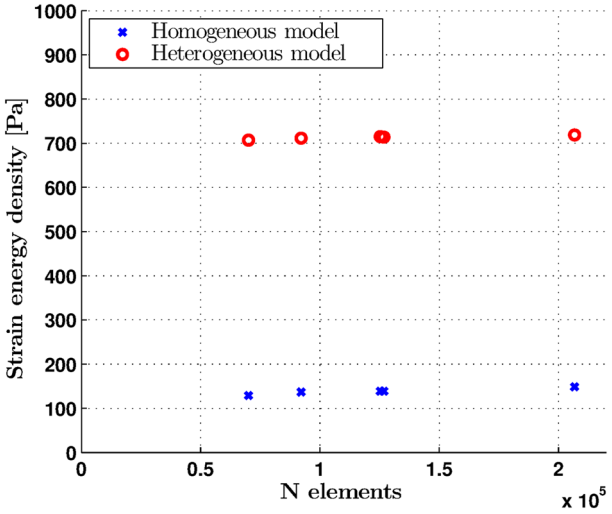

Figure 16. Convergence study: strain energy density averaged over all finite elements of the investigated finite elements mesh.

DOI: 10.1002/cnm

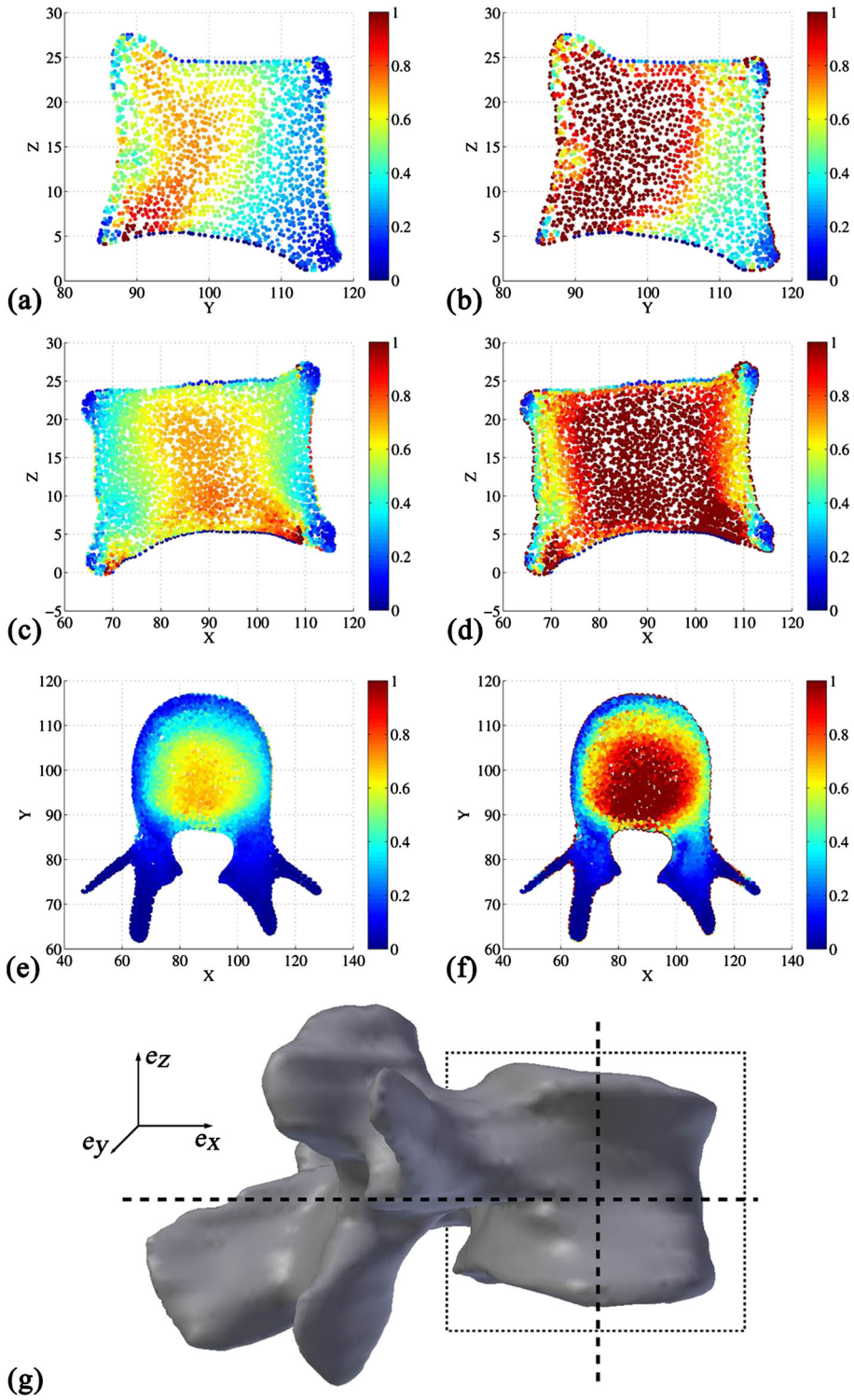

Figure 17. Maps of the 'yield loading degree' $1/\chi_y$, related to 1 MPa pressure loading; across the sagittal plane through the vertebral body, for (a) homogeneous, and (b) heterogeneous finite element model, across the coronal plane, for (c) homogeneous, and (d) heterogeneous finite element model; across the transverse plane, for (e) homogeneous, and (f) heterogeneous finite element model. (g) Three-dimensional representation of the organ and position of the slices. Cross-sectional dimensions are in millimeters.

DOI: 10.1002/cnm

Combination of the latter with the porosity maps illustrated in Figure 11 allows for assembly of mechanical property maps as depicted in Figure 15. The latter evidences the very inhomogeneous nature of the organ: The left side of the vertebra organ is less porous and, hence, denser and stiffer than its right-hand side. Feeding these properties into the differently fine finite element models

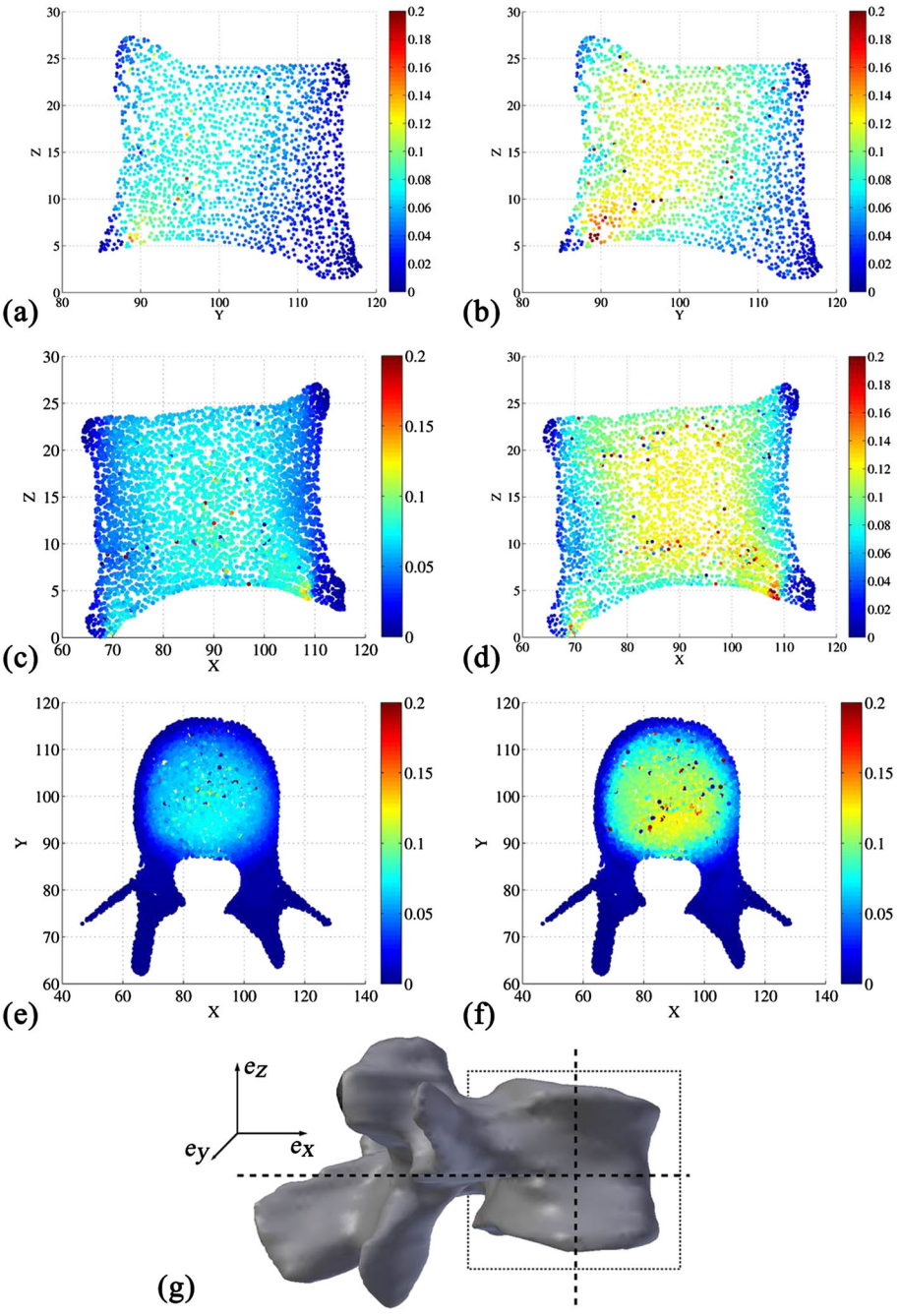

Figure 18. Maps of the 'ultimate loading degree' $1/\chi_{ult}$, related to 1 MPa pressure loading; across the sagittal plane through the vertebral body, for (a) homogeneous, and (b) heterogeneous finite element model; across the coronal plane, for (c) homogeneous, and (d) heterogeneous finite element model; across the transverse plane, for (e) homogeneous, and (f) heterogeneous finite element model. (g) Three-dimensional representation of the organ and position of the slices. Cross-sectional dimensions are in millimeters.

DOI: 10.1002/cnm

described in Section 2.6 and Figure 6 yields very similar results in terms of the strain energy density (Figure 16), which underlines the sufficient accuracy of the employed finite element meshes. This implies at the same time that the algorithm for using the minimum of three CT-based porosity values for characterizing one finite element (Section 2.6) delivers satisfactorily accurate results. However, there are truly significant differences between the homogeneous and heterogeneous simulations. Given the employed traction boundary conditions, this indicates that the homogeneous simulations by far overestimate the stiffness of the investigated organ. Stress levels obtained, under axial "physiological load", on both homogeneous and heterogeneous simulations reach the level of material yielding (Figure 17), more pronouncedly so in the heterogeneous simulations (compare Figure 17(a, c, and e) to Figure 17(b, d, and f)), while this load level is characterized by a 'safety factor'of about 10 (for homogeneous simulations) and 5 (for heterogeneous simulations) from material failure [compare Figure 18(a,c, and e) to (b,d, and f)]. Corresponding element-wise increase of the linear elastically determined stress tensors up to the level of material failure is evoking remarkably nonlinear strain evolutions, as is seen in Figure 19.

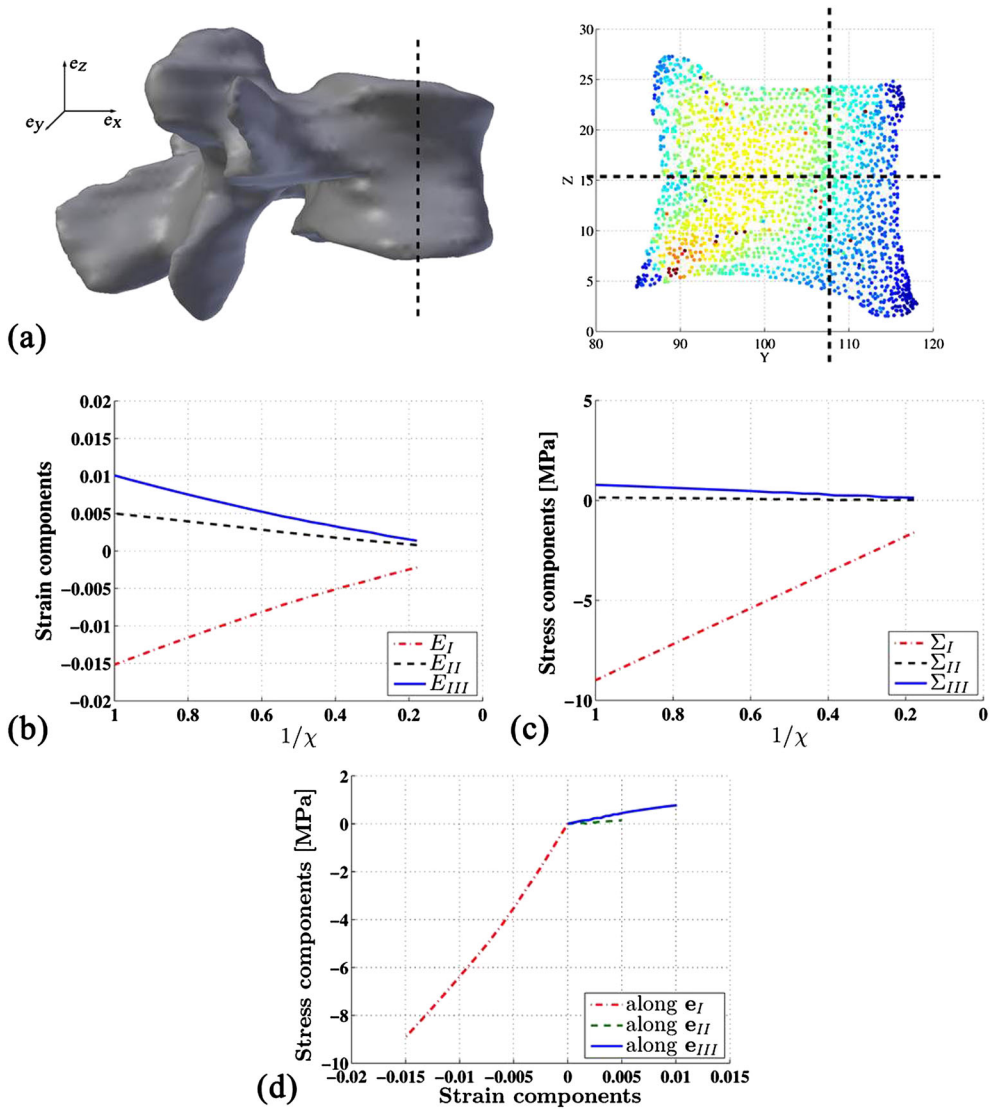

Figure 19. Proportional stress loading in chosen finite element (a), (b) principal stress components, (c) principal stress components as function of the loading degree, and (d) strain relation along principal directions.

DOI: 10.1002/cnm

4. DISCUSSION

Combining latest continuum micromechanics models with 'universal'composition and mineralization rules for bone, which both were successfully validated against a multitude of physically and statistically independent experimental data, and with X-ray physics and finite element modeling, allowed for patient-specific fracture-risk assessment of lumbar vertebrae. In this context, it should be emphasized that we here extended the patient specificity beyond purely geometric aspects, which are somehow defining the current state of the art in computational patient-specific analysis [135–139]; in fact, we here explicitly consider the patient-specific grey value distribution quantifying the spatial X-ray attenuation behavior of the scanned organs and convert the latter into patient-specific microstructural information. The latter then provides, via micromechanics analysis, patient-specific elasticity and strength distributions, which are finally mapped onto the patient-specific geometrical data that we started off with.

Secondly, it is very interesting and instructive to compare the results of our novel method, which is solely based on clinical CT data, with results from well established, say 'conventional', methods published in the open literature. These methods comprise Archimedes' principle, ultrasound, microCT, macromechanical testing, nanoindentation, and micro-finite element-based tissue elasticity determination.

To begin with, two different techniques, namely, Archimedes' principle and evaluation of clinical CT images based on energy-dependent, intravoxel attenuation averaging in conjunction with 'universal' compositional rules for soft and hard tissues, delivered the same extracellular bone mass density, when applied to two differently old human vertebrae characterized at two different hospitals. This strongly underlines the organ-specificity, but location and age independence of extracellular tissue properties (when averaged over one-to-several-millimeter-sized domains). This remarkable extracellular tissue characteristic is also evident from age-independent nanoindentation moduli on human proximal femora [140–142], as well as from age-independent and location-independent mineral contents, as obtained from computerized quantitative contact radiography of whole human iliac bone [143], as observed by means of quantitative backscattered electron imaging of iliac and vertebral trabecular samples [144], as seen under Raman microscopy of femoral cortices [145], or as investigated through a microCT of an entire human radius [146].

It may also be noteworthy that mass densities obtained *ex vivo*, from samples being stored in a frozen state with temperature and humidity conditions varying quite strongly from those *in vivo*, agree very well with the mass density data retrieved from *in vivo* scanning protocols. This, however, agrees very well with evidence put forward by a number of studies [147–150] that the mechanical properties of bone tissue are preserved through storage, also when bones are frozen. Because the mechanical properties of bone tissue depend on the tissue's composition and microstructure [30, 151], it appears as very natural that also the composition-related quantities, such as the tissue mass density, would not be more than negligibly affected by the storage and testing procedure. As a side result, this allowed us to do without human biopsies when validating our *in vivo* method. In fact, a biopsy from a young healthy patient was never considered for ethical reasons, thus ruling out intrusive measurement of the patient-specific bone mineral density. This is a normal situation for any analysis performed on clinical data, such as the ones reported by [152].

Agreement of our tissue mass density result with all these prior investigations nurtures the confidence in our new method, which delivers fully patient-specific and site-specific data on bone tissue composition, resolved down to the single voxel level. At this stage, it already drives forward the highly desired knowledge on local bone composition characteristics, as it was achieved by high-resolution peripheral quantitative computed tomography acquisition schemes on radial bones [65, 153, 154], delivering, as a result, bone mineral densities as averages over cortical or trabecular compartments, with values lying well within the ranges illustrated in Figures 12(a) and 13(b). Our method, however, while not being dependent on high-resolution peripheral quantitative computed tomography (which is only applicable to extremities), but just based on standard clinical CTs, gives not only compartment averages, but bone composition gradients resolved down to a voxel size of $0.324\times0.324\times1.25$ mm^3. The identified mass density of 1.67 g/cm^3 underlines that vertebral tissue is remarkably less dense than femoral or tibial tissue, with reported extracellullar mass densities

DOI: 10.1002/cnm

lying between 1.9 and 2.0 g/cm^3 [30, 55, 58]. This is consistent with ultrasonic waves traveling slower through vertebral as compared with femoral tissues [49].

Moreover, our mineral contents derived from *in vivo* CT data without the need of any type of phantom agree remarkably well with *ex vivo* quantitative CT studies as well as ashing studies on vertebral autopsies [155]: for an age slightly below 20 years, i.e. similar to the one of the patient investigated here, the latter reference reports bone mineral contents between 70 and 200 mg/cm^3 relating to a similarly aged patient, a range which well frames the mean value in Figure 12(a) and 13(b). Hence, we provided a new *in vivo* access to values for the so-called volumetric bone mineral density – vBMD. The latter are very valuable indicators for clinical decisions, as they have been shown to significantly correlate to the occurrence of bone fracture [156], that is, they are valuable indicators for bone fracture risk. However, such correlations [157–159] do not consider the wealth of knowledge on how materials break, as it has been gained in the fields of material physics and mechanics over centuries.

To the best knowledge of the authors, we here provided the first calibration-free, X-ray physics-based and multiscale mechanics-based fracture risk analysis tool applied to human vertebra, based on multiscale elastoplasticity. In this context, it is first interesting to compare the results of the multiscale model as depicted on Figure 5 with corresponding independent experimental results found in the open literature. Namely, the (average) axial normal stiffness component of extracellular bone matrix, amounting to 15.4 GPa, agrees virtually perfectly with the nanoindentation-derived value reported by Wolfram *et al*. [142], amounting also to 15.4 GPa. At the same time, we observe that the nanoindentation measurements may reveal, when using respective protocols [160], strictly speaking orthotropic material properties, while the micromechanical model employed herein is based on hexagonal symmetry and hence provides transversely isotropic properties. The question arises on how our approximation of orthotropy through transverse isotropy may influence the results of the type of analysis as reported herein. This question can be answered in two independent ways, leading to virtually the same answer. The first answer builds on computing the axial Young's modulus of a piece of orthotropic bone matrix from both the orthotropic stiffness tensor and from the transversely isotropic approximation of this stiffness tensor, as obtained from rotation around the axial material direction [161]. In the latter reference, it was shown the corresponding difference in axial Young's moduli computed for the orthotropic data of Ashman *et al*. [162] amounts to less than 1%, and the same is true for the analogous computations based on the data of [160]. Because only this (axial) Young's modulus enters our finite element analyses, we regard the latters' results to be almost entirely independent of the choice of transversely isotropic as compared with orthotropic material properties. The second answer relates to the reliability of formally isotropic analysis as described in Section 2.6: use of such formally isotropic properties as retrieved from the aforementioned nanoindentation campaign indeed delivered micro-finite element results, which agreed particularly well with direct test results of entire vertebrae in both compression and torsion [163]. This further increases the confidence into our method.

As regards the plastic load regime, our results for a human lumbar vertebra aged 15 years indicate plastic deformations to even occur under normal physiological loading agree well with the growing evidence of low-level plasticity in bone tissue, demonstrated by means of mechanical experiments and finite element simulations of trabecular bone [164, 165]. The safety factor against ultimate fracture is found to be around five, corresponding to an ultimate load amounting to 4614 N, which lies well within the broad range of values determined experimentally on different human vertebrae [1–4]. Our ultimate load particularly well agrees with the values of ultimate load measured on vertebrae of similar mean BMD [1, 3, 11], and for a bone of similar mean porosity [2, 10]. It is very interesting that our failure also agrees very well with those determined for femurs, both experimentally [16] and by means of finite element strength computations [17]. This indicates larger domains of the skeleton to be designed for bearing the same level of loading. Thereby, the critical load may well be attained in extreme sport activities, as compressive forces of 8676 N in the block action of an American football player, 7500 N during a golf swing, or 7756 N during torso weight lifting [166]. The question may arise whether the large regions close to yielding under kind of a 'light loading' make sense from an evolutionary biology standpoint. The answer may actually be affirmative, given the evolution of the spine as a lightweight shock absorbing organ system. In

DOI: 10.1002/cnm

fact, dissipative mechanical behavior of vertebral bone even under light loads seems very much consistent with spine's function as kind of a 'shock absorber'. Accordingly, even at low loading, the mechanical work put into the system would not be entirely recoverable upon unloading but be partially dissipated into heat. Identification of related yielding phenomena critically relies on the advanced multiscale formulation used herein, in order to describe the elastoplastic behavior of bone, in particular at the scale of the extracellular bone matrix. The plastic behavior of bone at low load levels at this small scale has been very recently shown also by a direct experimental method where single micron-sized samples glued onto a rigid substrate have been loaded and unloaded in the compressive regime [167]. A particular feature of our new method is the consistent consideration of heterogeneous elasticity and strength properties throughout the organ; it is remarkable that our bottom-up approach value for the Young's modulus of the extravascular space (see Equation (48)) compares well with data stemming from top-down back-computations reported in the literature [168], and the importance of heterogeneity for fracture loads has been repeatedly stated [169]. In our case, the heterogeneity results from the bone remodeling induced by the natural asymmetry of the human body, with the right part of the middle section of the vertebra being less porous, and therefore stiffer than the left-hand part; see Figure 11(b) and 15(a). Resulting stress concentrations govern the organ's compliance and safety margin against fracture: stiffness and strength properties based on an averaged homogeneous vascular porosity would overestimate the strain energy density by a factor of 5, and the safety factor by a factor of 2. This key role of tissue heterogeneity in the mechanics of the investigated biological system is fully consistent with similar earlier findings on a variety of other tissues, such as human and murine femoral bone [43, 170, 171], primate skull [172], human patellar cartilage [173], or human arterial wall tissue [174].

Our method critically depended on a successful micromechanial representations of bone microstructure for mechanical property predictions, which does not resolve the material up to the highest resolution ever possible, but rather focus on reliable consideration of the mechanically most important micromorphological features. While in the present case, the micromechanics model was set within the framework of continuum micromechanics or random homogenization theory, the same philosophy can also be followed within alternative theoretical frames, such as that of lattice models [113]. At the same time, our method impressively confirms the increasing expectations of the clinical environments with regard to advanced numerical methods, especially those based on the finite element method [175].

It is also appropriate to discuss potential limitations of the new method presented here. The phantom-free CT data evaluation critically relies on the existence of two distinguishable peaks in the histogram of grey values as depicted in Figure 7, these peaks being related to the adipose and the soft tissue, respectively. Certain pathological conditions or poor resolution images may render these two peaks as non-distinguishable. In this case, the scanning of the clinically interesting part of the body, together with a piece of material with known chemical composition (such as a phantom used for standard CT data calibration purposes) may deliver access to a second grey value with known corresponding attenuation coefficient, so that a system of equations similar to that of Equations (2) and (3) may again provide access to the energy-dependent functions $a(\mathcal{E})$ and $b(\mathcal{E})$. Such a 'phantom-based' X-ray energy determination process has been described in greater detail for ceramic biomaterials [44]. In its current formulation, the presented method is realized for the case if the cortical shell is thinner than the voxel size; see procedure of Section 2.2. This procedure would need modification if thick cortical shells, that is, such with thicknesses spanning one entire or even several voxels edge lengths, would appear in the scanned domain. Actually, the maximum grey value would then coincide with the extravascular grey value GV_{ev}, so that Equations (8) to (12) would become superfluous, while the rest of the analysis would stay unaltered.

The practical impact of our study is deemed to lie in its ability to allow for an enhanced exploitation of standard clinical CT data with low radiation exposure to the patient, thereby revealing information, which would otherwise stay unnoticed. Without any additional efforts with respect to standard medical examinations, the method described here allows for unprecedented information on the fracture risk of the scanned vertebrae. Such information may be deemed essential in the process of seeking a diagnosis or treatment processes [176].

DOI: 10.1002/cnm

As a side effect of the clinical orientation of our protocol (we are dealing with data from a living patient), the *in vivo* scanned object could not be used for further *in situ* testing. Still, the identified mass density agreed very well with that obtained from a cadaveric specimen. This agreement further confirms earlier statements on the temporal and spatial invariance of species-specific and organ-specific adult bone tissue mass density when averaged over millimeter-sized domains [37, 140–146].

Finally, one might discuss on how to proceed this research work so as to eventually integrate it into a real-life clinical setting. One administrative problem in this context could be the integration of commercial finite element software as employed here, together with several in-house codes produced at the university, in current workflow systems employed in the clinical everyday life; together with the software and hardware computer power needed for running advanced medium-scale finite element computations as reported herein. In this context, advanced computational techniques such as automated object-based image analysis [177], or statistical shape models for active feature selection [178], are gaining popularity. A more conceptually fundamental way to overcome the aforementioned challenge could be to substitute the full 3D finite element analyses by similarly precise, yet computationally and commercially less expensive advanced beam model solutions. In fact, preliminary work in our research group (which is obviously beyond the scope of the present paper) indicates that advanced 'sandwich beam'-type theories turn out as theoretically challenging, but highly effective alternatives to finite element models. They are particularly effective when it comes to tackling load cases, which go beyond the basic situation of a constant pressure acting on the upper boundary of the investigated vertebra as described in this paper. This can be already sketched here, in order to give a first-order approximation of how the safety factors would roughly change when a typical bending moment of some 40 Nm [179], in addition to the constant pressure of 1 MPa as discussed earlier, would be applied to the studied vertebra. Approximating the vertebral cross section as shown in Figure 9 as a homogeneous ellipse with some 50-mm width and 33-mm height results in a minimal area moment of inertia of $I=33^3 \times 50 \times \frac{\pi}{4}=1.4\times10^6$ mm^4, so that the normal stresses due to bending can be roughly estimated as $\sigma=40/(1.4\times10^{-6})\times16.5 \times 10^{-3} \approx 500 \times 10^3$ Pa$=$ 0.5 MPa. Hence, a typical bending mode on top of the compressive loading studied throughout this paper leads to an increase of the pseudo-uniaxial stress state of Figure 19 by around 30%, that is, the overall safety would be expected to be around four in combined axial-bending load.

5. CONCLUSION

Based on consistent integration of micromechanics, finite element analysis, and X-ray physics, conventional clinical CT data alone allow for reliable determination of tissue mass density and mineralization degree, as well as engineering mechanics-based fracture risk analysis considering both patient-specific loading and microstructurally governed conditions of mechanical integrity.

6. CONFLICT OF INTEREST STATEMENT

The authors Romane Blanchard, Claire Morin, Andrea Malandrino, Alain Vella, Zdenka Sant, and Christian Hellmich hereby declare that they have no conflict of interest.

ACKNOWLEDGEMENTS

The grey value-to-composition conversion scheme development was financially supported through project MySPINE, grant number 269909 of EC call FP7-ICT-2009-6. Collaboration with the University of Malta and Mater Dei Hospital, Malta, was supported through grant NAMABIO, MPNS Action COST MP1005. Completion of the strength model became possible through project MICROBONE, Grant number 257023, granted by the European Research Council (ERC). Moreover, the authors gratefully acknowledge the support of Manfred Tschabitscher from the Center of Anatomy and Cell Biology at the Medical University of Vienna, providing a vertebra for the mass density tests. The latter were performed as part of a 2010 internship of Andrea Malandrino from the Institute of Bioengineering of Catalonia (IBEC), Biomechanics and Mechanobiology Group (headed by Damien Lacroix until 2012, and by Jerome Noailly since 2012), at Vienna University of Technology, which was made possible through the bilateral Austro-Spanish scientific exchange grant ES06/2010 AT2009-0029. CT scanning of the aforementioned vertebra was provided by

DOI: 10.1002/cnm

Heinz Redl from the Ludwig Boltzmann Institute for Clinical and Experimental Traumatology, in the framework of the Austrian Cluster for Tissue Regeneration.

REFERENCES

1. Cheng X, Nicholson P, Boonen S, Lowet G, Brys P, Aerssens J, van der Perre G, Dequeker J. Prediction of vertebral strength in vitro by spinal bone densitometry and calcaneal ultrasound. *Journal of Bone and Mineral Research* 1997; **12**(10):1721–1728.
2. Perilli E, Briggs AM, Kantor S, Codrington J, Wark JD, Parkinson IH, Fazzalari NL. Failure strength of human vertebrae: prediction using bone mineral density measured by dxa and bone volume by micro-CT. *Bone* 2012; **50**(6):1416–1425.
3. Crawford RP, Rosenberg WS, Keaveny TM. Quantitative computed tomography-based finite element models of the human lumbar vertebral body: effect of element size on stiffness, damage, and fracture strength predictions. *Journal of Biomechanical Engineering* 2003; **125**:434–438.
4. McBroom RJ, Hayes WC, Edwards WT, Goldberg RP, White AA. Prediction of vertebral body compressive fracture using quantitative computed tomography. *The Journal of Bone and Joint Surgery. American volume* 1985; **67**: 1206–1214.
5. Melton III LJ, Atkinson EJ, O'Fallon WM, Wahner HW, Riggs BL. Long-term fracture prediction by bone mineral assessed at different skeletal sites. *Journal of Bone and Mineral Research* 1993; **8**(10):1227–1233.
6. Black DM, Steinbuch M, Palermo L, Dargent-Molina P, Lindsay R, Hoseyni MS, Johnell O. An assessment tool for predicting fracture risk in postmenopausal women. *Osteoporosis International* 2001; **12**(7):519–528.
7. Hulme PA, Boyd SK, Ferguson SJ. Regional variation in vertebral bone morphology and its contribution to vertebral fracture strength. *Bone* 2007; **41**:946–957.
8. Singer K, Edmondston S, Day R, Breidahl P, Price R. Prediction of thoracic and lumbar vertebral body compressive strength: correlations with bone mineral density and vertebral region. *Bone* 1995; **17**(2):167–174.
9. Hutton WC, Cyron BM, Stott JR. The compressive strength of lumbar vertebrae. *Journal of Anatomy* 1979; **129**(4):753–758.
10. Jiang G, Luo J, Pollintine P, Dolan P, Adams Ma, Eastell R. Vertebral fractures in the elderly may not always be 'osteoporotic'. *Bone* 2010; **47**(1):111–6.
11. Ebbesen EN, Thomsen JS, Beck-Nielsen H, Nepper-Rasmussen HJ, Mosekilde Li. Lumbar vertebral body compressive strength evaluated by dual-energy X-ray absorptiometry, quantitative computed tomography, and ashing. *Bone* 1999; **25**:713–724.
12. Rockhoff SD, Sweet E, Bleustein J. The relative contribution of trabecular and cortical bone to the strength of human lumbar vertebrae. *Calcified Tissue Research* 1969; **3**:163–175.
13. Cody DD, Gorss GJ, Hou FJ, Spencer HJ, Goldstein SA, Fyhrie DP. Femoral strength is better predicted by finite element models than QCT and DXA. *Journal of Biomechanics* 1999; **32**:1013–1020.
14. MacNeil JA, Boyd SK. Bone strength at the distal radius can be estimated from high-resolution peripheral quantitative computed tomography and the finite element method. *Bone* 2008; **42**(6):1203–1213.
15. Keyak JH, Rossi SA, Jones KA, Skinner HB. Prediction of femoral fracture load using automated finite element modeling. *Journal of Biomechanics* 1998; **31**(2):125–133.
16. Schileo E, Taddei F, Cristofolini L, Viceconti M. Subject-specific Finite Element models implementing a maximum principal strain criterion are able to estimate failure risk and fracture location on human femurs tested *in vitro*. *Journal of Biomechanics* 2008; **41**:356–367.
17. Falcinelli C, Schileo E, Balistreri L, Baruffaldi F, Bordini B, Viceconti M, Albisinni U, Ceccarelli F, Milandri L, Toni A, Taddei F. Multiple loading conditions analysis can improve the association between finite element bone strength estimates and proximal femur fractures: A preliminary study in elderly women. *Bone* 2014; **67**:71–80.
18. Yosibash Z, Padan R, Joskowicz L, Milgrom C. A CT-based high-order finite element analysis of the human proximal femur compared to in-vitro experiments. *Journal of Biomechanical Engineering* 2007; **129**(3):297–309.
19. Trabelsi N, Yosibash Z. Patient-specific finite-element analyses of the proximal femur with orthotropic material properties validated by experiments. *Journal of Biomechanical Engineering* 2011; **133**(6).
20. Trabelsi N, Milgrom C, Yosibash Z. Patient-specific FE analyses of metatarsal bones with inhomogeneous isotropic material properties. *Journal of the Mechanical Behavior of Biomedical Materials* 2014; **29**:177–189.
21. Morgan EF, Bayraktar HH, Keaveny TM. Trabecular bone modulus-density relationships depend on anatomic site. *Journal of Biomechanics* 2003; **36**(7):897–904.
22. Keyak JH, Lee IY, Skinner HB. Correlations between orthogonal mechanical properties and density of trabecular bone: Use of different densitometric measures. *Journal of Biomedical Materials Research* 1994; **28**(11):1329–1336.
23. Goulet RW, Goldstein SA, Ciarelli MJ, Kuhn JL, Brown MB, Feldkamp LA. The relationship between the structural and orthogonal compressive properties of trabecular bone. *Journal of Biomechanics* 1994; **27**(4):375–389.
24. Rho JY, Hobatho MC, Ashman RB. Relations of mechanical properties to density and CT numbers in human bone. *Medical Engineering & Physics* 1995; **17**(5):347–355.
25. Périé D, Sales de Gauzy J, Baunin C, Hobatho MC. Tomodensitometry measurements for in vivo quantification of mechanical properties of sciolotic vertebrae. *Clinical Biomechanics* 2001; **16**:373–379.
26. Natali AN, Carniel EL, Pavan PG. Investigation of bone inelastic response in interaction phenomena with dental implants. *Dental Materials* 2008; **24**(4):561–569.

DOI: 10.1002/cnm

27. Geraldes DM, Phillips ATM. A comparative study of orthotropic and isotropic bone adaptation in the femur. *International Journal for Numerical Methods in Biomedical Engineering* 2014; **30**:873–889.
28. Frost HM. Bone Mass and the Mechanostat : A Proposal. *The Anatomical Record* 1987; **219**:1–9.
29. Hellmich C, Ulm F, Dormieux L. Can the diverse elastic properties of trabecular and cortical bone be attributed to only a few tissue-independent phase properties and their interactions? Arguments from a multiscale approach. *Biomechanics and Modeling in Mechanobiology* 2004; **2**(4):219–238.
30. Vuong J, Hellmich Ch. Bone fibrillogenesis and mineralization: Quantitative analysis and implications for tissue elasticity. *Journal of Theoretical Biology* 2011; **287**:115–130.
31. Morin C, Hellmich C, Henits P. Fibrillar structure and elasticity of hydrating collagen: a quantitative multiscale approach. *Journal of Theoretical Biology* 2013; **317**:384–393.
32. Morin C, Hellmich C. Mineralization-driven bone tissue evolution follows from fluid-to-solid phase transformations in closed thermodynamic systems. *Journal of Theoretical Biology* 2013; **335**:185–197.
33. Fritsch A, Hellmich C. 'Universal' microstructural patterns in cortical and trabecular, extracellular and extravacular bone materials: micromechanics-based prediction of anisotropic elasticity. *Journal of Theoretical Biology* 2007; **244**:597–620.
34. Fritsch A, Hellmich C, Dormieux L. Ductile sliding between mineral crystals followed by rupture of collagen crosslinks: experimentally supported micromechanical explanation of bone strength. *Journal of Theoretical Biology* 2009; **260**:230–252.
35. Morin C, Hellmich C. A multiscale poromicromechanical approach to wave propagation and attenuation in bone. *Ultrasonics* 2014; **54**(5):1251–1269.
36. Hubbell JH, Seltzer SM. *Tables of X-ray mass attenuation coefficients and mass energy-absorption coefficients from 1 keV to 20 MeV for elements Z = 1 to 92 and 48 additional substances of dosimetric interest*, 2011. http://www.nist.gov/pml/data/xraycoef/index.cfm/.
37. Hellmich C, Kober C, Erdmann B. Micromechanics-based conversion of CT data into anisotropic elasticity tensors, applied to FE simulations of a mandible. *Annals of Biomedical Engineering* 2008; **36**(1):108–122.
38. Crawley EO, Evans WD, Owen GM. A theoretical analysis of the accuracy of single-energy CT bone measurements. *Physics in Medicine and Biology* 1988; **33**(10):1113–1127.
39. Jackson DF, Hawkes DJ. X-ray attenuation coefficients of elements and mixtures. *Physics Reports* 1981; **70**(3):169–233.
40. Yosibash Z, Trabelsi N, Hellmich C. Subject-specific p-FE analysis of the proximal femur utilizing micromechanics-based material properties. *International Journal for Multiscale Computational Engineering* 2008; **6**(5):483–498.
41. Scheiner S, Sinibaldi R, Pichler B, Komlev V, Renghini C, Vitale-Brovarone C, Rustichelli F, Hellmich C. Micromechanics of bone tissue-engineering scaffolds, based on resolution error-cleared computer tomography. *Biomaterials* 2009; **30**:2411–2419.
42. Dejaco A, Komlev VS, Jaroszewicz J, Swieszkowski W, Hellmich C. Micro CT-based multiscale elasticity of double-porous (pre-cracked) hydroxyapatite granules for regenerative medicine. *Journal of Biomechanics* 2012; **45**(6):1068–1075.
43. Blanchard R, Dejaco A, Bongaers E, Hellmich C. Intravoxel bone micromechanics for microct-based finite element simulations. *Journal of Biomechanics* 2013; **46**(15):2710–2721.
44. Czenek A, Blanchard R, Dejaco A, Sigurjónsson OE, Örlygsson G, Gargiulo P, Hellmich C. Quantitative intravoxel analysis of microCT-scanned resorbing ceramic biomaterials - perspectives for computer-aided biomaterial design. *Journal of Materials Research* 2014; **29**(23):2757–2772.
45. Medical Imaging and Technology Alliance (division of the National Electrical Manufacturers Association): DICOM PS3.3 2013-Information Object Definitions (2013).
46. Mast TD. Empirical relationships between acoustic parameters in human soft tissues. *Acoustics Research Letters Online* 2000; **1**(2):37–42.
47. Lees S. Considerations regarding the structure of the mammalian mineralized osteoid from viewpoint of the generalized packing model. *Connective Tissue Research* 1987; **16**(4):281–303.
48. Gautieri A, Buehler MJ, Redaelli A. Deformation rate controls elasticity and unfolding pathways of single tropocollagen molecules. *Journal of the Mechanical Behavior of Biomedical Materials* 2009; **2**:130–137.
49. Malandrino A, Fritsch A, Lahayne O, Kropik K, Redl H, Noailly J, Lacroix D, Hellmich C. Anisotropic tissue elasticity in human lumbar vertebra, by means of a coupled ultrasound-micromechanics approach. *Materials Letters* 2012; **78**:154–158.
50. Silva MJ, Wang C, Keaveny TM, Hayes WC. Direct and computed tomography thickness measurements of the human, lumbar vertebral shell and endplate. *Bone* 1994; **15**(4):409–414.
51. Whitehouse WJ, Dyson ED, Jackson CK. The scanning electron microscope in studies of trabecular bone from a human vertebral body. *Journal of Anatomy* 1971; **108**(3):481–496.
52. Ritzel H, Amling M, Pösl M, Hahn M, Delling G. The thickness of human vertebral cortical bone and its changes in aging and osteoporosis: a histomorphic analysis of the complete spinal column from thirty-seven autopsy specimen. *Journal of Bone and Mineral Research* 1997; **12**(1):89–95.
53. Lees S, Cleary PF, Heeley JD, Gariepy EL. Distribution of sonic plesio-velocity in a compact bone sample. *Journal of the Acoustical Society of America* 1979; **66**(3):641–646.
54. Lees S, Hanson D, Page E. Some acoustical properties of theotic bones of a fin whale. *Journal of the Acoustical Society of America* 1995; **99**(4):2421–2427.

DOI: 10.1002/cnm

55. Lees S, Ahern JM, Leonard M. Parameters influencing the sonic velocity in compact calcified tissues of various species. *Journal of the Acoustical Society of America* 1983; **74**(1):28–33.
56. Lees S. Mineralization of type I collagen. *Biophysical Journal* 2003; **85**:204–207.
57. Lees S, Page EA. A study of some properties of mineralized turkey leg tendon. *Connective Tissue Research* 1992; **28**(4):263–287.
58. Biltz RM, Pellegrino ED. The chemical anatomy of bone. I. A comparative study of bone composition in sixteen vertebrates. *Journal of Bone and Joint Surgery - Series A* 1969; **51**(3):456–466.
59. Gong JK, Arnold JS, Cohn SH. Composition of trabecular and cortical bone. *The Anatomical Record* 1964; **149**: 325–332.
60. Burns CM. XCIV. The effect of the continued ingestion of mineral acid on growth of body and bone and on the composition of bone and of the soft tissues. *Biochemical Journal* 1929; **23**(5):860–867.
61. Hammett FS. A biochemical study of bone growth. I. Changes in the ash, organic matter and water during growth (mus norvegicus albinus). *Journal of Biological Chemistry* 1925; **64**:409–428.
62. Hammett FS. Studies of the thyroid apparatus: XIV. The growth of the humerus and femur of male and female albino rats thyro-parathyroidectomized and parathyroidectomized when 100 days of age. *The Journal of Experimental Zoology* 1924; **39**(3):465–504.
63. Chick H, Korenchevsky V, Roscoe M. LXXXIII. The difference in chemical composition of the skeletons of young rats fed (1) on diets deprived of fat-soluble vitamins and (2) on a low phosphorus rachitic diet, compared with those of normally nourished animals of same age. *Biochemical Journal* 1926; **20**(3):621–631.
64. Tai K, Pelled G, Sheyn D, Bershteyn A, Han L, Kallai I, Zilberman Y, Ortiz C, Gazit D. Nanobiomechanics of repair bone regenerated by genetically modified mesenchymal stem cells. *Tissue Engineering: Part A* 2008; **14**(10): 1709–1720.
65. Neu CM, Manz F, Rauch F, Merkel A, Schoenau E. Bone density and bone size at the distal radius in healthy children and adolescents: a study using peripheral quantitative computed tomography. *Bone* 2001; **28**(2):227–232.
66. Urist MR, DeLange RJ, Finerman GAM. Bone cell differentiation and growth factors. *Science* 1983; **220**:680–686.
67. Hellmich C, Barthélémy JF, Dormieux L. Mineral-collagen interactions in elasticity of bone ultrastructure – a continuum micromechanics approach. *European Journal of Mechanics A-Solids* 2004; **23**:783–810.
68. McCarthy RN, Jeffcott LB, McCartney RN. Ultrasound speed in equine cortical bone: effects of orientation, density, porosity and temperature. *Journal of Biomechanics* 1990; **23**(11):1139–1143.
69. Lees S, Hanson D, Page EA, Mook HA. Comparison of dosage-dependent effects of beta-aminopropionitrile, sodium fluoride, and hydrocortisone on selected physical properties of cortical bone. *Journal of Bone and Mineral Research* 1994; **9**(9):1377–1389.
70. Lees S. Ultrasonic measurements of deer antler, bovine tibia and tympanic bulla. *Journal of Biomechanics* 1982; **15**(11):867–874.
71. Hellmich C, Ulm FJ. Average hydroxyapatite concentration is uniform in extracollageneous ultrastructure of mineralized tissue. *Biomechanics and Modeling in Mechanobiology* 2003; **2**:21–36.
72. Zylberberg L, Traub W, de Buffrenil V, Allizard F, Arad T, Weiner S. Rostrum of a toothed whale: ultrastructural study of a very dense bone. *Bone* 1998; **23**:241–247.
73. Prostak KS, Lees S. Visualization of crystal-matrix structure. In situ demineralization of mineralized turkey leg tendon and bone. *Calcified Tissue International* 1996; **59**:474–479.
74. Lees S. Water content in type I collagen tissues calculated from the generalized packing model. *International Journal of Biological Macromolecules* 1986; **8**:66–72.
75. Bonar L, Lees S, Mook H. Neutron diffraction studies of collagen in fully mineralized bone. *Journal of Molecular Biology* 1985; **181**:265–270.
76. Lees S, Bonar LC, Mook HA. A study of dense mineralized tissue by neutron diffraction. *International Journal of Biological Macromolecules* 1984; **6**(6):321–326.
77. Hodge AJ, Petruska JA. Recent studies with the electron microscope on ordered aggregates of the tropocollagen molecule. In *Aspects of protein structure – proceedings of a symposium held in madras 14 - 18 january 1963 and organized by the university of madras, india*, Ramachandran GN (ed.). Academic Press: London and New York, 1963; 289–300.
78. Meek KM, Fullwood NJ, Cooke PH, Elliott GF, Maurice DM, Quantock aJ, Wall RS, Worthington C R. Synchrotron X-ray diffraction studies of the cornea, with implications for stromal hydration. *Biophysical journal* 1991; **60**(2):467–74.
79. Bergman I, Loxley R. Two improved and simplified methods for the spectrophotometric determination of hydroxyproline. *Analytical Chemistry* 1963; **35**(12):1961–1965.
80. Rougvie M, Bear R. An X-ray diffraction investigation of swelling by collagen. *Journal of the American Leather Chemists Association* 1953; **48**(12):735–751.
81. Grosso VAD, Mader CW. Speed of sound in pure water. *Journal of the Acoustical Society of America* 1972; **52**(5B):1442–1446.
82. Sant Z, Cauchi M, Spiteri M. Analysis of stress-strain distribution within a spinal segment. *Journal of Mechanics of Materials and Structures* 2012; **7**(3):255–263.
83. Wang Y, Battié MC, Boyd SK, Videman T. The osseous endplates in lumbar vertebrae: thickness, bone mineral density and their associations with age and disk degeneration. *Bone* 2011; **48**(4):804–809.
84. Yoganandan N, Mykiebust JB, Cusick JF, Wilson CR, Jr AS. Functional biomechanics of the thoracolumbar vertebral cortex. *Clinical Biomechanics* 1988; **3**(1):11–18.

85. Rietbergen BV, Odgaard A, Kabel J, Huiskes R. Direct mechanics assessment of elastic symmetries and properties of trabecular bone architecture. *Journal of Biomechanics* 1996; **29**(12):1653–1657.
86. Cowin SC. Remarks on the paper entitled 'fabric and elastic principal directions of cancellous bone are closely related'. *Journal of Biomechanics* 1997; **30**(11/12):1191–1192.
87. Bhowmik R, Katti K, Katti DR. Mechanics of molecular collagen is influenced by hydroxyapatite in naturial bone. *Journal of Materials Science* 2007; **42**:8824–8837.
88. Bhowmik R, Katti KS, Katti DR. Mechanisms of load-deformation behavior of molecular collagen in hydroxyapatite-tropocollagen molecular system: steered molecular dynamics study. *Journal of Engineering Mechanics* 2009; **135**(5):413–421.
89. Wilson EE, Awonusi A, Kohn MD, Tecklenburg MMJ, Beck LW. Three structural roles for water in bone observed by solid-state NMR. *Biophysical Journal* 2006; **90**:3722–3731.
90. Pan H, Tao J, Tang R. Molecular simulation of water behaviors on crystal faces of hydroxyapatite. *Frontiers of Chemistry in China* 2007; **2**(2):156–163.
91. Zahn D, Hochrein O. Computational study of interfaces between hydroxyapatite and water. *Physical Chemistry Chemical Physics* 2003; **5**:4004–4007.
92. Catanese J, Iverson EP, Ng RK, Keaveny TM. Heterogeneity of the mechanical properties of demineralized bone. *Journal of Biomechanics* 1999; **32**:1365–1369.
93. Christiansen DL, Huang EK, Silver FH. Assembly of type I collagen: fusion of fibril subunits and the influence of fibril diameter on mechanical properties. *Matrix Biology* 2000; **19**:409–420.
94. Gentleman E, Lay AN, Dickerson DA, Neuman EA, Livesay GA, Dee KC. Mechanical characterization of collagen fibers and scaffolds for tissue engineering. *Biomaterials* 2003; **24**:3805–3813.
95. Burstein AH, Currey JD, Frankel VH, Reilly DT. The ultimate properties of bone tissue: the effects of yielding. *Journal of Biomechanics* 1972; **5**:35–44.
96. Burstein AH, Zika JM, Heiple KG, Klein L. Contribution of collagen and mineral to the elastic-plastic properties of bone. *The Journal of Bone and Joint Surgery. American volume* 1975; **57**:956–961.
97. Burstein AH, Reilly DT, Martens M. Aging of bone tissue: mechanical properties. *The Journal of Bone and Joint Surgery. American volume* 1976; **58**:82–86.
98. Cezayirlioglu H, Bahniuk E, Davy DT, Heiple KG. Anisotropic yield behavior of bone under combined axial force and tension. *Journal of Biomechanics* 1985; **18**(1):61–69.
99. Currey JD. Differences in the tensile strength of bone of different histological types. *Journal of Anatomy* 1959; **93**:87–95.
100. Currey JD. The effects of strain rate, reconstruction and mineral content on some mechanical properties of bovine bone. *Journal of Biomechanics* 1975; **8**:81–86.
101. Currey JD. Physical characteristics affecting the tensile failure properties of compact bone. *Journal of Biomechanics* 1990; **23**:837–844.
102. Currey JD. Tensile yield in compact bone is determined by strain, post-yield behaviour by mineral content. *Journal of Biomechanics* 2004; **37**(4):549–556.
103. Dickenson RP, Hutton WC, Stott JR. The mechanical properties of bone in osteoporosis. *The Journal of Bone and Joint Surgery. British volume* 1981; **63-B**:233–238.
104. Hellmich Ch, Müllner HW, Kohlhauser Ch. Mechanical (triaxial) tests on biological materials and biomaterials. *Technical Report DNRT3-1.2-3*, Network of excellence 'Knowledge-based Multicomponent Materials for Durable and Safe Performance –KMM-NoE', sponsored by the European Commission, 2006.
105. Kotha S P, Guzeslu N. Modeling the tensile mechanical behavior of bone along the longitudinal direction. *Journal of Theoretical Biology* 2002; **219**:269–279.
106. Lee SC, Coan BS, Bouxsein ML. Tibial ultrasound velocity measured in situ predicts the material properties of tibial cortical bone. *Bone* 1997; **21**:119–125.
107. Martin RB, Burr DB. *Structure, function, and adaptation of compact bone*. Raven Press: New York, NY, USA, 1989.
108. Reilly DT, Burstein AH, Frankel VH. The elastic modulus for bone. *Journal of Biomechanics* 1974; **7**:271–275.
109. Reilly DT, Burstein AH. The elastic and ultimate properties of compact bone tissue. *Journal of Biomechanics* 1975; **8**:393–405.
110. Riggs CM, Vaughan LC, Evans GP, Lanyon LE, Boyde A. Mechanical implications of collagen fibre orientation in cortical bone of equine radius. *Anatomy and Embryology* 1993; **187**:239–248.
111. Evans FG, Lebow M. The strength of human compact bone as revealed by engineering technics. *American Journal of Surgery* 1952; **83**(3):326–31.
112. Walsh WR, Guzelsu N. Ion concentration effects on bone streaming potentials and zeta potentials. *Biomaterials* 1993; **14**(5):331–336.
113. Diamant I, Shahar R, Masharawi Y, Gefen A. A method for patient-specific evaluation of vertebral cancellous bone strength: in vitro validation. *Clinical Biomechanics* 2007; **22**(3):282–291.
114. Katz J.L., Ukraincik K. On the anisotropic elastic properties of hydroxyapatite. *Journal of Biomechanics* 1971; **4**:221–227.
115. Fritsch A, Dormieux L, Hellmich C, Sanahuja J. Mechanical behaviour of hydroxyapatite biomaterials: an experimentally validated micromechanical model for elasticity and strength. *Journal of Biomedical Materials Research* 2009; **88A**:149–161.
116. Akao M, Aoki H, Kato K. Mechanical properties of sintered hydroxyapatite for prosthetic applications. *Journal of Materials Science* 1981; **16**:809–812.

DOI: 10.1002/cnm

117. Shareef MY, Messer PF, Noort Rv. Fabrication, characterization and fracture study of a machinable hydroxyapatite ceramic. *Biomaterials* 1993; **14**(1):69–75.
118. Liu DM. Preparation and characterisation of porous hydroxyapatite bioceramic via a slip-casting route. *Ceramics International* 1998; **24**(6):441–446.
119. Charrière E, Terrazzoni S, Pittet C, Mordasini P, Dutoit M, Lemaître J, Zysset P. Mechanical characterization of brushite and hydroxyapatite cements. *Biomaterials* 2001; **22**:2937–2945.
120. Arita IH, Wilkinson DS, Mondragón MA, Castaño VM. Chemistry and sintering behaviour of thin hydroxyapatite ceramics with controlled porosity. *Biomaterials* 1995; **16**:403–408.
121. Peelen JGJ, Rejda BV, de Groot K. Preparation and properties of sintered hydroxylapatite. *Ceramurgia International* 1978; **4**:71–74.
122. De With G, van Dijk H, Hattu N, Prijs K. Preparation, microstructure and mechanical properties of dense polycrystalline hydroxyapatite. *Journal of Materials Science* 1981; **16**:1592–1598.
123. Martin RI, Brown PW. Mechanical properties of hydroxyapatite formed at physiological temperature. *Journal of Materials Science: Materials in Medicine* 1995; **6**:138–143.
124. Simo JC, Hughes TJR. *Computational inelasticity,* Interdisciplinary Applied Mathematics, vol. 7. Springer-Verlag: New York, 1998.
125. Melan E. Zur Plastizität des räumlichen Kontinuums. *Ingenieur-Archiv* 1938; **9**(2):116–126.
126. Zaoui A. Continuum micromechanics: survey. *Journal of Engineering Mechanics (ASCE)* 2002; **128**(8):808–816.
127. Hill R. Elastic properties of reinfored solids: some theoretical principles. *Journal of the Mechanics and Physics of Solids* 1963; **11**:357–362.
128. Hashin Z. Analysis of composite materials – a survey. *Journal of Applied Mechanics (ASME)* 1983; **50**(3):481–503.
129. Levin VM. Thermal expansion coefficient of heterogeneous materials. *Mekhanika Tverdogo Tela* 1967; **2**(1): 83–94.
130. Pichler B, Hellmich C. Estimation of influence tensors for eigenstresses multiphase elastic media with nonaligned inclusion phases of arbitrary ellipsoidal shape. *Journal of Engineering Mechanics* 2010; **136**(8):1043–1053.
131. Fritsch A, Hellmich C, Young P. Micromechanics-derived scaling relations for poroelasticity and strength of brittle porous polycrystals. *Journal of Applied Mechanics, Transactions ASME* 2013; **80**(2).
132. Badel PB, Leblond JB. A note on integration schemes for the microplane model of the mechanical behaviour of concrete. *Communications in Numerical Methods in Engineering* 2004; **20**(1):75–81.
133. Simo JC, Taylor RL. Consistent tangent operators for rate-independent elastoplasticity. *Computer Methods in Applied Mechanics and Engineering* 1985; **48**(1):101–118.
134. Clausen J, Damkilde L, Andersen L. Efficient return algorithms for associated plasticity with multiple yield planes. *International Journal for Numerical Methods in Engineering* 2006; **66**(6):1036–1059.
135. Pant S, Fabrèges B, Gerbeau JF, Vignon-Clementel I E. A methodological paradigm for patient-specific multi-scale CFD simulations: from clinical measurements to parameter estimates for individual analysis. *International Journal for Numerical Methods in Biomedical Engineering* 2014; **30**(12):1614–16 48.
136. Onishi Y, Aoki K, Amaya K, Shimizu T, Isoda H, Takehara Y, Sakahara H, Kosugi T. Accurate determination of patient-specific boundary conditions in computational vascular hemodynamics using 3D cine phase-contrast MRI. *International Journal for Numerical Methods in Biomedical Engineering* 2013; **29**(10):1089–1103.
137. Liang F, Sughimoto K, Matsuo K, Liu H, Takagi S. Patient-specific assessment of cardiovascular function by combination of clinical data and computational model with applications to patients undergoing Fontan operation. *International Journal for Numerical Methods in Biomedical Engineering* 2014; **30**(10):1000–1018.
138. Boileau E, Bevan RLT, Sazonov I, Rees MI, Nithiarasu P. Flow-induced ATP release in patient-specific arterial geometries – a comparative study of computational models. *International Journal for Numerical Methods in Biomedical Engineering* 2013; **29**(10):1038–1056.
139. Arzani A, Les AS, Dalman RL, Shadden SC. Effect of exercise on patient specific abdominal aortic aneurysm flow topology and mixing. *International Journal for Numerical Methods in Biomedical Engineering* 2014; **30**(2): 280–295.
140. Hoffler CE, Moore KE, Kozloff K, Zysset PK, Goldstein SA. Age, gender, and bone lamellae elastic moduli. *Journal of Orthopaedic Research* 2000; **18**:432–437.
141. Rho JY, Zioupos P, Currey JD, Pharr GM. Microstructural elasticity and regional heterogeneity in human femoral bone of various ages examined by nano-indentation. *Journal of Biomechanics* 2002; **35**:189–198.
142. Wolfram U, Wilke HJ, Zysset PK. Rehydration of vertebral trabecular bone: influences on its anisotropy, its stiffness and the indentation work with a view to age, gender and vertebral level. *Bone* Febuary 2010; **46**(2):348–54.
143. Boivin G, Meunier PJ. The degree of mineralization of bone tissue measured by computerized quantitative contact microradiography. *Calcified Tissue International* 2002; **70**:503–511.
144. Roschger P, Gupta HS, Berzlanovich A, Ittner G, Dempster DW, Fratzl P, Cosman F, Parisien M, Lindsay R, Nieves JW, Klaushofer K. Constant mineralization density distribution in cancellous human bone. *Bone* 2003; **32**:316–323.
145. Akkus O, Polyakova-Akkus A, Adar F, Schaffler MB. Aging of microstructural compartments in human compact bone. *Journal of Bone and Mineral Research* 2003; **18**(6):1012–1019.
146. Bossy E, Talmant M, Peyrin F, Akrout L, Cloetens P, Laugier P. In in vitro study of the ultrasonic axial transmission technique at the radius: 1 MHz velocity measurements are sensitive to both mineralization and introcortical porosity. *Journal of Bone and Mineral Research* 2004; **19**(9):1548–1556.
147. Panjabi MM, Krag M, Summers D, Videman T. Biomechanical time-tolerance of fresh cadaveric human spine specimens. *Journal of Orthopaedic Research* 1985; **3**(3):292–300.

148. Linde F, Christian H, Sorensen F. The effect of different storage methods on the mechanical properties of trabecular bone. *Journal of Biomechanics* 1993; **26**(10):1249–1252.
149. Nazarian A, Hermannsson BJ, Muller J, Zurakowski D, Snyder BD. Effects of tissue preservation on murine bone mechanical properties. *Journal of Biomechanics* 2009; **42**(1):82–86.
150. Fölsch C, Mittelmeier W, Bilderbeek U, Timmesfeld N, Von Garrel T, Matter HP. Effect of storage temperature on allograft bone. *Transfusion Medicine and Hemotherapy* 2012; **39**(1):36–40.
151. Fritsch A, Hellmich C. Universal' microstructural patterns in cortical and trabecular, extracellular and extravacular bone materials: Micromechanics-based prediction of anisotropic elasticity. *Journal of Theoretical Biology* 2007; **244**:597–620.
152. Castro I, Humbert L, Whitmarsh T, Lazary A, Del Rio Barquero LM, Frangi AF. 3D reconstruction of intervertebral discs from T1-weighted magnetic resonance images. *2012 9th IEEE International Symposium on Biomedical Imaging (ISBI)* 2012:1695–1698.
153. Hasegawa K, Hasegawa Y, Nagano A. Estimation of bone mineral density and architectural parameters of the distal radius in hemodialysis patients using peripheral quantitative computed tomography. *Journal of Biomechanics* 2004; **37**(5):751–756.
154. Nishiyama KK, Macdonald HM, Moore S, Fung T, Boyd SK, McKay H. Cortical porosity is higher in boys compared with girls at the distal radius and distal tibia during pubertal growth: an HR-pQCT study. *Journal of Bone and Mineral Research* 2012; **27**(2):273–82.
155. Ebbesen EN, Thomsen JS, Beck-Nielsen H, Nepper-Rasmussen HJ, Mosekilde L. Vertebral bone density evaluated by dual-energy X-ray absorptiometry and quantitative computed tomography in vitro. *Bone* 1998; **23**(3):283–90.
156. Lang TF, Guglielmi G, van Kuijk C, De Serio A, Cammisa M, Genant HK. Measurement of bone mineral density at the spine and proximal femur by volumetric quantitative computed tomography and dual-energy X-ray absorptiometry in elderly women with and without vertebral fractures. *Bone* 2002; **30**(1):247–250.
157. Wachter NJ, Augat P, Mentzel M, Sarkar MR, Krischak GD, Kinzl L, Claes LE. Predictive value of bone mineral density and morphology determined by peripheral quantitative computed tomography for cancellous bone strength of the proximal femur. *Bone* 2001; **28**(1):133–139.
158. Yu WS, Chan KY, Yu FWP, Ng BKW, Lee KM, Qin L, Lam TP, Cheng JCY. Bone structural and mechanical indices in adolescent idiopathic scoliosis evaluated by high-reolution peripheal quantitative computed tomography (HR-pQCT). *Bone* 2014; **61**:109–115.
159. Melton III LJ, Riggs BL, van Lenthe GH, Achenbach SJ, Müller R, Bouxsein ML, Amin S, Atkinson EJ, Khosla S. Contribution of in vivo structural measurements and load/strength ratios to the determination of forearm fracture risk in postmenopausal women. *Journal of Bone and Mineral Research* 2007; **22**(9):1442–1448.
160. Franzoso G, Zysset PK. Elastic anisotropy of human cortical bone secondary osteons measured by nanoindentation. *Journal of Biomechanical Engineering* 2009; **131**(2):021001.
161. Yoon YJ, Yang G, Cowin SC. Estimation of the effective transversely isotropic elastic constants of a material from known values of the material's orthotropic elastic constants. *Biomechanics and Modeling in Mechanobiology* 2002; **1**(1):83–93.
162. Ashman RB, Cowin SC, Van Buskirk WC, Rice JC. A continuous wave technique for the measurement of the elastic properties of cortical bone. *Journal of Biomechanics* 1984; **17**(5):349–361.
163. Wolfram U, Wilke HJ, Zysset PK. Valid micro finite element models of vertebral trabecular bone can be obtained using tissue properties measured with nanoindentation under wet conditions. *Journal of Biomechanics* June 2010; **43**(9):1731–1737.
164. Kelly N, Harrison NM, McDonnell P, McGarry JP. An experimental and computational investigation of the post-yield behaviour of trabecular bone during vertebral device subsidence. *Biomechanics and Modeling in Mechanobiology* 2013; **12**(4):685–703.
165. Schwiedrzik J, Raghavan R, Bürki A, LeNader V, Wolfram U, Michler J, Zysset P. In situ micropillar compression reveals superior strength and ductility but an absence of damage in lamellar bone. *Nature materials* 2014; **13**: 740–747.
166. Gatt CJ, Hosea TM, Palumbo RC, Zawadsky JP. Impact loading of the lumbar spine during football blocking. *American Journal of Sports Medicine* 1997; **25**(3):317–321.
167. Luczynski KW, Steiger-Thirsfeld A, Bernardi J, Eberhardsteiner J, Hellmich Christian. Extracellular bone matrix exhibits hardening elastoplasticity and more than double cortical strength: evidence from homogeneous compression of non-tapered single micron-sized pillars welded to a rigid substrate. *Journal of the Mechanical Behavior of Biomedical Materials* 2015; **52**:51–62.
168. Bevill G, Keaveny TM. Trabecular bone strength predictions using finite element analysis of micro-scale images at limited spatial resolution. *Bone* 2009; **44**(4):579–584.
169. Bürklein D, Lochmüller E, Kuhn V, Grimm J, Barkmann R, Müller R, Eckstein F. Correlation of thoracic and lumbar vertebral failure loads with in situ vs. ex situ dual energy X-ray absorptiometry. *Journal of Biomechanics* 2001; **34**(5):579–587.
170. Baca V, Horak Z, Mikulenka P, Dzupa V. Comparison of an inhomogeneous orthotropic and isotropic material models used for fe analyses. *Medical Engineering and Physics* 2008; **30**:924–930.
171. Schneider R, Faust G, Hindenlang U, Helwig P. Inhomogeneous, orthotropic material model for the cortical structure of long bones modelled on the basis of clinical CT or density data. *Computer Methods in Applied Mechanics and Engineering* 2009; **198**(27-29):2167–217.

DOI: 10.1002/cnm

172. Wroe S, Moreno K, Clausen P, McHenry C, Curnoe D. High-resolution three-dimensional computer simulation of homonid cranial mechanics. *The Anatomical Record* 2007; **290**:1248–1255.
173. Pierce DM, Ricken T, Holzapfel GA. Modeling sample/patient-specific structural and diffusional responses of cartilage using DT-MRI. *International Journal for Numerical Methods in Biomedical Engineering* 2013; **29**(8): 807–821.
174. Decorato I, Kharboutly Z, Vassallo T, Penrose J, Legallais C, Salsac AV. Numerical simulation of the fluid structure interactions in a compliant patient-specific arteriovenous fistula. *International Journal for Numerical Methods in Biomedical Engineering* 2014; **30**(2):143–159.
175. Sievaenen. Bone densitometry and true BMD accuracy for predicting fractures : what are the alternatives? Review. *International Journal of Clinical Rheumatology* 2010; **5**(3):371–385.
176. Epstein NE. Are recommended spine operations either unnecessary or too complex? Evidence from second opinions. *Surgical Neurology International* 2013; **4**(Suppl 5):S353–S358.
177. Schwier M, Chitiboi T, Hülnhagen T, Hahn HK. Automated spine and vertebrae detection in CT images using object-based image analysis. *International Journal for Numerical Methods in Biomedical Engineering* 2013; **29**(9):938–963.
178. Castro-Mateos I, Pozo J, Lazary A, Frangi A. 3D Vertebra Segmentation by Feature Selection Active Shape Model. In *Recent advances in computational methods and clinical applications for spine imaging*, vol. 20, Yao J, Glocker B, Klinder T, Li S (eds)., Lecture Notes in Computational Vision and Biomechanics. Springer International Publishing: Switzerland, 2015; 241–245.
179. Adams MA, Dolan P. A technique for quantifying the bending moment acting on the lumbar spine in vivo. *Journal of Biomechanics* January 1991; **24**(2):117–126.

NOMENCLATURE

Variables
a... slope of linear relation between grey values and X-ray attenuation coefficients
A... area
$\mathbb{A}$... strain concentration tensor
b... intercept of linear relation between grey values and X-ray attenuation coefficients
$\mathbb{C}$... stiffness tensor
C_{ijkl}... stiffness tensor component
C^{-1}_{ijkl}... compliance tensor component
$\mathbb{D}_{ic,\Phi\Theta}$... influence tensor accounting for the influence of plastic strains in the $(\Phi\Theta)$-oriented mineral phase on the total strains in the inter-crystalline pores
$\mathbb{D}_{\phi\theta\Phi\Theta}$... influence tensor accounting for the influence of plastic strains in the $(\Phi\Theta)$-oriented mineral phase on the total strains in the $(\phi\theta)$-oriented phase
E... Young's modulus
$\mathcal{E}$... photon energy
$\mathbf{E}$... macroscopic strain
f_i^j... volume fraction of phase i (if specified, in the RVE j; otherwise, in the macroscopic RVE)
$\mathcal{F}$... yield function
$\mathcal{G}$... flow potential
G_i... shear modulus of constituent i
GV... X-ray attenuation-related grey value
$\mathbb{I}$... fourth-order identity tensor
k_i... bulk modulus of constituent i
l... characteristic length
N_n... total number of finite elements
N_C... number of constituents in the volume (voxel)
$\mathbb{P}$... Hill tensor or morphological tensor
R... ratio
RVE ... representative volume element
V_n... volume of the n-th finite element
W... weight
$\mathbf{x}$... (microscopic) position vector inside the RVE

DOI: 10.1002/cnm

β... ratio between compressive and tensile yield stress of hydroxyapatite
δ_{ij}... Kronecker delta
$\boldsymbol{\varepsilon}$... microscopic strain tensor
$\dot{\lambda}$... plastic multiplier
μ_i... X-ray intensity attenuation coefficient of constituent i
ν... Poisson's ratio
$\boldsymbol{\xi}$... displacement
ρ_i... "real" mass density of material constituent i
$\rho_i^{*,j}$... apparent mass density of material constituent i per volume of space j
$\overline{\rho}$... average mass density
$\boldsymbol{\sigma}$... microscopic stress
$\boldsymbol{\Sigma}$... macroscopic stress
ϕ_i^j... porosity of space i (if specified, in the RVE j; otherwise, in the macroscopic RVE)
χ... risk factor
ψ... macroscopic strain energy density
$\overline{\psi}$... strain energy density averaged over organ

Subscripts
1... in radial direction
2... in circumferential direction
3... in axial direction
a... dried in air
$bone$... of bone
col... of collagen
$cort$... of cortical shell
cyl... of cylindrical inclusions
dev... deviatoric part
ec... of extracellular bone matrix
ef... of the extrafibrillar space
end... of the bony endplate
ev... at extravascular scale
fat... of adipose tissues
HA... of hydroxyapatite
H_2O... of water
$H_2O + ncp$... of water and non-collageneous proteins
hom... homogenized
ic... of the inter-crystalline space
lac... of lacunae
$macro$... of macroscopic bone
max... maximum value
$max - 1$... penultimate maximum value
org... of organic matter
$organ$... of the full organ
s... submerged in water
$soft$... of soft tissues
sph... of spherical inclusions
thr... at threshold value
vas... of vascular porosity
vol... volumetric part
$voxel$... of one voxel of the computed tomography image
ult... ultimate
y... at the start of yielding

DOI: 10.1002/cnm

$\phi, \theta, \Phi, \Theta$... Euler angles defining the orientation of the crystal needles (cylindrical mineral phases)

Superscripts
I, II, III... eigenvalues
ec... in the extracellular bone RVE
ef... in the extrafibrillar space
EV... statistically expected value
iso... in an isotropic phase
p... plastic
$trab$... of trabecular bone
ult... ultimate
up... upscaled
y... at the start of yielding

Mathematical symbols
∇^s... symmetrized nabla operator
:... second-order tensor contraction

DOI: 10.1002/cnm